



**AFRL-RX-WP-TP-2010-4072**

# **MEASUREMENT AND INTERPRETATION OF FLOW STRESS DATA FOR THE SIMULATION OF METAL- FORMING PROCESSES (Preprint)**

**S.L. Semiatin**

**Processing Section  
Metals Branch**

**T. Altan**

**The Ohio State University**

**JANUARY 2010  
Interim Report**

**Approved for public release; distribution unlimited.**

*See additional restrictions described on inside pages*

**STINFO COPY**

**AIR FORCE RESEARCH LABORATORY  
MATERIALS AND MANUFACTURING DIRECTORATE  
WRIGHT-PATTERSON AIR FORCE BASE, OH 45433-7750  
AIR FORCE MATERIEL COMMAND  
UNITED STATES AIR FORCE**

# REPORT DOCUMENTATION PAGE

*Form Approved  
OMB No. 0704-0188*

The public reporting burden for this collection of information is estimated to average 1 hour per response, including the time for reviewing instructions, existing data sources, gathering and maintaining the data needed, and completing and reviewing the collection of information. Send comments regarding this burden estimate or any other aspect of this collection of information, including suggestions for reducing this burden, to Department of Defense, Washington Headquarters Services, Directorate for Information Operations and Reports (0704-0188), 1215 Jefferson Davis Highway, Suite 1204, Arlington, VA 22202-4302. Respondents should be aware that notwithstanding any other provision of law, no person shall be subject to any penalty for failing to comply with a collection of information if it does not display a currently valid OMB control number. **PLEASE DO NOT RETURN YOUR FORM TO THE ABOVE ADDRESS.**

<b>1. REPORT DATE (DD-MM-YY)</b>  January 2010			<b>2. REPORT TYPE</b>  Journal Article Preprint	<b>3. DATES COVERED (From - To)</b>  01 January 2010 – 01 January 2010
<b>4. TITLE AND SUBTITLE</b> MEASUREMENT AND INTERPRETATION OF FLOW STRESS DATA FOR THE SIMULATION OF METAL-FORMING PROCESSES (Preprint)			<b>5a. CONTRACT NUMBER</b> IN HOUSE  <b>5b. GRANT NUMBER</b>  <b>5c. PROGRAM ELEMENT NUMBER</b> 62102F	
<b>6. AUTHOR(S)</b> S.L. Semiatin (Metals Branch, Processing Section (AFRL/RXLMP)) T. Altan (The Ohio State University)			<b>5d. PROJECT NUMBER</b> 4347  <b>5e. TASK NUMBER</b> RG  <b>5f. WORK UNIT NUMBER</b> M02R2000	
<b>7. PERFORMING ORGANIZATION NAME(S) AND ADDRESS(ES)</b>  Processing Section (AFRL/RXLMP) Metals Branch , Metals, Ceramics, and Nondestructive Evaluation Division Materials and Manufacturing Directorate, Air Force Research Laboratory Wright-Patterson Air Force Base, OH 45433-7750 Air Force Materiel Command, United States Air Force			<b>8. PERFORMING ORGANIZATION REPORT NUMBER</b> The Ohio State University  AFRL-RX-WP-TP-2010-4072	
<b>9. SPONSORING/MONITORING AGENCY NAME(S) AND ADDRESS(ES)</b>  Air Force Research Laboratory Materials and Manufacturing Directorate Wright-Patterson Air Force Base, OH 45433-7750 Air Force Materiel Command United States Air Force			<b>10. SPONSORING/MONITORING AGENCY ACRONYM(S)</b> AFRL/RXLMP	
			<b>11. SPONSORING/MONITORING AGENCY REPORT NUMBER(S)</b> AFRL-RX-WP-TP-2010-4072	
<b>12. DISTRIBUTION/AVAILABILITY STATEMENT</b> Approved for public release; distribution unlimited.				
<b>13. SUPPLEMENTARY NOTES</b> PAO case number 88 ABW-2009-4136, cleared 23 September 2009. This work was funded in whole or in part by Department of the Air Force work unit M02R2000. The U.S. Government has for itself and others acting on its behalf an unlimited, paid-up, nonexclusive, irrevocable worldwide license to use, modify, reproduce, release, perform, display, or disclose the work by or on behalf of the U. S. Government. To be published in the ASM Handbook, Volume 22B, Modeling and Simulation: Processing of Metallic Materials. Paper contains color.				
<b>14. ABSTRACT</b> Slip activity, Burgers vector populations, and dislocation densities were determined by X-ray line-profile analysis of peaks from individual grains in a bulk polycrystalline sample. The method was tested at the focused X-ray beamline ID11 at the European Synchrotron Research Facility (ESRF) in Grenoble, France and was applied to a bulk commercial-purity titanium specimen for which slip activity was determined for 49 single grains. The most-active slip systems were of $<a>$ and $<c+a>$ type, and the orientation of the stresses acting on these slip systems revealed a spread due to the effect of neighborhood grains on plastic response. The new x-ray method can provide input for crystal-plasticity analyses and permits experimental verification of the results of numerical calculations which was not possible before.				
<b>15. SUBJECT TERMS</b> slip activity, Burgers vector populations, dislocation densities, polycrystalline sample				
<b>16. SECURITY CLASSIFICATION OF:</b> a. REPORT Unclassified		<b>17. LIMITATION OF ABSTRACT:</b> b. ABSTRACT Unclassified c. THIS PAGE Unclassified SAR	<b>18. NUMBER OF PAGES</b> 64	<b>19a. NAME OF RESPONSIBLE PERSON</b> (Monitor) Sheldon L. Semiatin  <b>19b. TELEPHONE NUMBER</b> (Include Area Code) N/A

# Measurement and Interpretation of Flow Stress Data for the Simulation of Metal-Forming Processes

S.L. Semiatin\* and T. Altan\*\*

\* Air Force Research Laboratory, Materials & Manufacturing Directorate, WPAFB, OH

\*\*The Ohio State University, Columbus, OH

The yield stress of a metal under uniaxial conditions is often referred to as the “flow stress”. Metal starts to deform plastically when the applied stress (in uniaxial tension without necking or in uniaxial compression without bulging) reaches the value of the yield or flow stress. Metals which undergo flow hardening or softening exhibit an increasing or decreasing flow stress, respectively, with increasing strain. Furthermore, many metals show a small or large dependence of flow stress on both strain rate and temperature at cold or hot working temperatures, respectively. The quantification of flow stress constitutes one of the most important inputs to the simulation of a metal-forming process.

The flow stress of a metal may be quantified in terms of its dependence on strain, strain rate, and temperature. Such an approach yields a *phenomenological* description of flow behavior and is useful primarily for the specific material condition/microstructure and deformation regime in which actual measurements have been made. Alternatively, flow stress models can be based on so-called internal state variables such as dislocation density, grain size, phase fraction, strain rate, and temperature. In this case, the flow behavior can sometimes be extrapolated beyond the regime of measurements provided the deformation mechanism is unchanged. Irrespective of whether flow stress is described phenomenologically or mechanistically, similar measurement techniques are used.

For a given microstructural condition, the flow stress  $\bar{\sigma}$  can be expressed as a function of the strain  $\bar{\epsilon}$ , the strain rate,  $\dot{\bar{\epsilon}}$ , and the temperature  $T$ :<sup>1</sup>

$$\bar{\sigma} = f(T, \bar{\epsilon}, \dot{\bar{\epsilon}}) \quad (1)$$

During hot forming of metals (at temperatures above approximately one-half of the melting point), the effect of strain on flow stress is often weak and the influence of strain rate (i.e., rate of deformation) becomes increasingly important. Conversely, at room temperature (i.e., during cold forming), the effect

---

<sup>1</sup> Under uniaxial stress conditions, the axial stress  $\sigma$ , axial strain  $\epsilon$ , and axial strain rate  $\dot{\epsilon}$  are equal to the effective stress  $\bar{\sigma}$ , effective strain  $\bar{\epsilon}$ , and effective strain rate  $\dot{\bar{\epsilon}}$ . This is no longer true for multiaxial states of stress. Hence, effective quantities are used more often to represent flow stress because of their general applicability.

of strain rate on flow stress is usually small. The degree of dependence of flow stress on temperature varies considerably among different materials. Therefore, temperature variations during the forming process can have different effects on load requirements and metal flow for different materials.

To be useful in the analysis of a forming process, the flow stress of a metal should be determined experimentally for the strain, strain rate, and temperature conditions that exist during the process and for the specific microstructural condition of the workpiece material. The most commonly used methods for determining flow stress are the tension, uniform compression, and torsion tests [1].

## Tension Test

The tension test is commonly used to determine the mechanical (service) properties of metals. It is less frequently used to determine the large-strain flow stress of metals due the occurrence of necking at relatively small strains. Nevertheless, it does find application for the modeling of sheet-forming processes under ambient-temperature conditions (in which deformations can be moderate) and superplastic-forming operations at elevated temperatures in which a large value of the strain-rate-sensitivity exponent delays necking to large strains.

Two methods of representing flow stress data from the tension test are illustrated in Figure 1 [2]. In the classical *engineering*, or nominal, stress-strain diagram (Figure 1a), the engineering stress  $S$  is obtained by dividing the instantaneous tensile load,  $L$ , by the *original* cross-sectional area of the specimen,  $A_o$ . The stress  $S$  is then plotted against the engineering strain,  $e = (l - l_o)/l_o$ . During deformation, the specimen elongates initially in a uniform fashion. When the load reaches its maximum value, necking starts and the uniform uniaxial stress condition ceases to exist. Deformation is then concentrated in the neck region while the rest of the specimen undergoes very limited deformation.

Figure 1b illustrates the *true* stress-strain representation of the same tension-test data. In this case, before necking occurs, the following relationships are valid:

$$\begin{aligned}
 \bar{\sigma} &= \text{true stress (flow stress)} \\
 &= \text{instantaneous load/ instantaneous area} \\
 &= L/A \\
 &= S(1+e)
 \end{aligned} \tag{2}$$

and

$$\bar{\varepsilon} = \text{true strain} = \ln\left(\frac{l}{l_0}\right) = \ln\left(\frac{A_o}{A}\right) = \ln(1+e) \quad (3)$$

Prior to necking, the instantaneous load is given by  $L = A \bar{\sigma}$ . The criterion for necking can be formulated as the condition that  $L$  be maximum or that:

$$\frac{dL}{d\bar{\varepsilon}} = 0 \quad (4)$$

Furthermore, prior to the attainment of maximum load, the uniform deformation conditions (Equations (2) and (3)) are valid [2], and the following useful relations can be derived:

$$A = A_o e^{-\bar{\varepsilon}}$$

and

$$L = A \bar{\sigma} = A_o \bar{\sigma} e^{-\bar{\varepsilon}} \quad (5)$$

Combining Equations (4) and (5) results in:

$$\frac{dL}{d\bar{\varepsilon}} = 0 = A_o \left( \frac{d\bar{\sigma}}{d\bar{\varepsilon}} e^{-\bar{\varepsilon}} - \bar{\sigma} e^{-\bar{\varepsilon}} \right) \quad (6)$$

or

$$\frac{d\bar{\sigma}}{d\bar{\varepsilon}} = \bar{\sigma} \quad (7)$$

Very often the flow stress curve (or simply flow curve) obtained at room temperature can be expressed in the form of a power law relation between stress and strain, i.e.,

$$\bar{\sigma} = K \bar{\varepsilon}^n \quad (8)$$

in which  $K$  and  $n$  are material constants known as the strength coefficient and strain-hardening exponent, respectively. Combining Equations (7) and (8) results in:

$$\frac{d\bar{\sigma}}{d\bar{\varepsilon}} = K n (\bar{\varepsilon})^{n-1} = \bar{\sigma} = K (\bar{\varepsilon})^n \quad (9)$$

or

$$\bar{\varepsilon} = n \quad (10)$$

The condition expressed by Equation (7) is shown schematically in Figure 2. From this figure and Equation (10), it is evident that at low forming temperatures (for which Equation (8) is valid), a material with a large  $n$  has greater formability, i.e., it sustains a large amount of uniform deformation in tension, than a material with a smaller  $n$ . It should be noted, however, that this statement is not true for materials and conditions for which the flow stress cannot be expressed by Equation (8). Such is the

case at elevated (hot-working) temperatures at which the material response is very rate sensitive but often exhibits limited strain hardening.

The determination of flow stress after the onset of necking (Figure 1b) requires a correction because a triaxial state of stress is induced (Figure 3). Such a correction for a *round-bar* specimen, derived by Bridgman [3], is given by:

$$\bar{\sigma} = \frac{L}{\pi r^2} \left[ \left( 1 + \frac{2R}{r} \right) \ln \left( 1 + \frac{r}{2R} \right) \right]^{-1} \quad (11)$$

The quantities  $r$  and  $R$  are defined in Figure 3. For the evaluation of Equation (11), the values of  $r$  and  $R$  must be measured continuously during the test. A similar expression was also derived by Bridgman to determine the flow stress during necking of *sheet* tension samples.

## Uniaxial Compression Test

The compression test can be used to determine flow stress data for metals over a wide range of temperatures and strain rates. In this test, flat platens and a cylindrical sample are heated and maintained at the same temperature so that die chilling, and its influence on metal flow, is prevented. To be applicable without corrections or errors, the cylindrical sample must be upset without any barreling; i.e., the state of uniform stress in the sample must be maintained (Figure 4). Barreling is prevented by using adequate lubrication. Teflon, molybdenum sulfide, or machine oil is often used at room temperature. At hot working temperatures, graphite in oil is used for aluminum alloys, and melted glass is used for steel, titanium, and high-temperature alloys. To hold the lubricant, spiral grooves are often machined on both the flat surfaces of cylindrical test specimens (Figure 5a). The load and displacement (or sample height) are measured during the test. From this information, the average pressure is calculated at each stage of deformation, i.e., for increasing axial strain.

For frictionless, perfectly uniform compression, the average pressure-axial stress curve is equivalent to the flow curve. In this case, similar to the uniform elongation portion of the tension test, the following relationships are valid:

$$\bar{\varepsilon} = \ln \frac{h_o}{h} = \ln \frac{A}{A_o} \quad (12)$$

$$\bar{\sigma} = \frac{L}{A} \quad (13)$$

$$A = A_o e^{\bar{\varepsilon}} \quad (14)$$

$$\dot{\bar{\varepsilon}} = \frac{d\bar{\varepsilon}}{dt} = \frac{dh}{h dt} = \frac{v}{h} \quad (15)$$

in which  $v$  is instantaneous crosshead speed,  $h_0$  and  $h$  are the initial and instantaneous sample heights, respectively, and  $A_0$  and  $A$  are initial and instantaneous cross-sectional areas, respectively. Typically, the compression test can be conducted without barreling to ~50 pct. height reduction ( $\bar{\varepsilon} = 0.69$ ) or more. A typical load-displacement curve and the corresponding  $\bar{\sigma}$ - $\bar{\varepsilon}$  curve obtained for the uniform compression of annealed aluminum 1100 at room temperature is shown in Figure 6.

At hot working temperatures (i.e., temperatures typically in excess of one half of the absolute melting point), the flow stress of nearly all metals is very strain-rate dependent. Therefore, hot compression tests should be conducted using a test machine that provides a constant true strain rate; i.e., a constant value of the ratio of the crosshead speed to the instantaneous sample height (Equation (15)). For this purpose, programmable servohydraulic testing machines or cam plastometers are commonly used. Sometimes, a mechanical press is employed; however, an approximately constant strain rate is obtained for only the first half of the deformation when using such equipment. In order to maintain nearly isothermal and uniform compression conditions, hot compression tests are conducted in a furnace or using a preheated fixture such as that shown in Figure 7. The dies are coated with an appropriate lubricant; e.g., oil or graphite for temperatures to 800°F (425°C) and glass for temperatures to 2300°F (1260°C). The fixture/dies and the specimen are heated to the test temperature, soaked for a predetermined time (usually ~10-15 minutes), and then the test is initiated. Examples of tested hot compression samples are shown in Figure 8. Examples of high-temperature  $\bar{\sigma}$ - $\bar{\varepsilon}$  data are given in Figure 9.

### **Specimen Preparation**

There are two machining techniques that can be used for preparing specimens for the cylinder-compression test, viz., the spiral-groove design (Figure 5a) and the Rastegaev specimen (Figure 5b). The spiral grooves and the recesses of the Rastegaev specimen serve the purpose of retaining the lubricant at the tool-workpiece interface during compression, thus minimizing barreling. It has been determined that Rastegaev specimens provide better lubrication and hold their form better during testing compared to the spiral-grooved specimens. The specifications for the specimens and the test conditions are as follows [4]:

### Specimen with spiral grooves (Figure 5a)

Solid cylinder (diameter =  $0.5^{\pm 0.001}$  in., length =  $0.75^{\pm 0.005}$  in.).

Ends should be flat and parallel within 0.0005 in./in.

Surface should be free of grooves, nicks and burrs.

Spiral grooves machined at the flat ends of the specimen with approximately 0.01 in. depth.

### Rastegaev specimen (Figure 5b)

Flat recesses at the ends should be filled with lubricant.

Dimensions  $t_0 = 0.008^{\pm 0.0005}$  in. and  $u_0 = 0.02^{\pm 0.0005}$  in. at the end faces have a significant effect on the lubrication conditions.

Rastegaev specimen ensures good lubrication up to high strains of ~0.8 to 1; i.e., the specimen remains cylindrical due to the radial pressure that the lubricant exerts on the ring.

$t_0/u_0 = 0.4$  for steels (optimum value at which the specimen retains cylindrical shape up to maximum strain before bulging occurs).

### ***Parallelism of the Press (or Testing Machine) Dies***

In a compression test, load is applied on the billet using flat dies. In order to ensure that a uniaxial state of stress exists during the experiment, the applied load should be exactly parallel to the axis of the cylindrical specimen. This calls for measurement of the parallelism of the platens of the testing machine or press. A commonly used technique for measuring parallelism involves compressing lead billets of the same height as the test samples; lead is used because it is soft and deforms easily at room temperature. The circumferential variation in billet height is an indication of the parallelism of the platens. Alternatively, for large-diameter dies, lead samples can be placed at different locations. The difference in the final height of the samples following compression can be used to correct for parallelism.

### ***Errors in the Compression Test***

Errors in the determination of flow stress by the compression test can be classified in three categories [4]:

- Errors in the displacement readings, which result in errors in the calculated strain
- Errors in the load readings, which result in errors in the calculated stress
- Errors in the processing of the data due to barreling of the test specimens

The first and second type errors may be reduced or eliminated by careful calibration of the transducers and data acquisition equipment. However, barreling of the test specimens during compression cannot be entirely eliminated because there is always friction between the specimen and the tooling. The maximum error in determining flow stress via compression testing is thus usually that associated with friction. In order to correct the flow curve and to determine the percentage error in flow stress, finite-element-method (FEM) analysis is often used.

Average pressure ( $p_{av}$ ) - axial strain ( $\epsilon$ ) plots derived from measured load-stroke data (corrected for the test-machine compliance) and reduced assuming uniform deformation can also be corrected for friction effects using the following approximate relation [7]:

$$\frac{\bar{\sigma}}{p_{av}} = \left(1 + \frac{m_s d_s}{(3\sqrt{3})h}\right)^{-1}, \quad (16)$$

in which  $m_s$  denotes the friction shear factor determined from a ring test (described next), and  $d_s$  and  $h$  represent the instantaneous sample diameter and height, respectively.

### **Gleeble Systems**

Gleeble systems can be used to conduct hot/warm compression or tension tests on different specimen geometries. The Gleeble 3500 system uses direct resistance heating capable of heating the specimen at a rate up to 10,000°C/s. A high cooling rate of 10,000°C/s can be achieved using an optional quench system. Temperature measurements are done using thermocouples or an infrared pyrometer. The Gleeble 3500 mechanical system has a complete integrated hydraulic servo system capable of exerting maximum tensile/compressive (static) forces of 10 tons. It also has Windows-based software for running the test and analyzing the data.

### **Ring Test**

The ring test consists of compressing a flat ring shaped specimen to a known reduction (Figure 10). Changes in the external and internal diameters of the ring are very dependent on the friction at the tool/specimen interface [5]. If the friction were equal to zero, the ring would deform in the same way as a solid disk, with each element flowing radially outward at a rate proportional to its distance from the center. With increasing deformation, the internal diameter of the ring is reduced if friction is large and is increased if friction is low. Thus, the change in the internal diameter represents a simple method for evaluating interface friction.

The ring test can be used to quantify friction in terms of either an interface friction shear factor  $m_s$  ( $= \sqrt{3}(\tau/\bar{\sigma})$ , in which  $\tau$  denotes the interface shear stress) or a Coulomb coefficient of friction  $\mu$ . In either case, a numerical simulation of the ring test is conducted for the specific ring geometry, workpiece/die temperatures, and a range of friction factors/coefficients of friction to generate a series of so-called calibration curves describing the dependence of the percentage decrease in the ring ID on height reduction. Corresponding measured values of the ID decrease (or increase) for several different height reductions are cross plotted on the set of calibration curves to determine the pertinent friction factor/coefficient of friction; the ID measurements are made at the internal bulge A typical set of calibration curves for ring tests under isothermal conditions (die and workpiece at the same temperature) and various ring geometries (i.e., ratios of initial ring OD: ring ID: thickness) are shown in Figure 11.

## Plane-Strain Compression Test

The plane-strain compression test (Figure 12) was developed to establish stress-strain curves for the rolling process. According to Watts and Ford [8], the ratio of the width of the plate  $b$  to its thickness  $h$  should be greater than 6 (i.e.,  $b/h > 6$ ) in order to ensure plane-strain compression. The recommended value of  $b/h$  should be at least 10 [9]. The ratio between breadth of the tool and the plate thickness  $h$  should satisfy the inequality  $2 < a/h < 4$  [10].

During the test, one starts with a tool whose breadth is twice the initial thickness of the strip. This tool pair is used to compress the specimen to half of its thickness. Then, the tool is exchanged with second tool with half the breadth of the first tool and compression goes on until the sheet is one-fourth its original thickness. A tool with one-half the breadth of the second can be inserted and so on. Thus a plane strain compression test can be carried out keeping  $a/h$  between the recommended limits [10].

The equivalent strain in the plane-strain compression test is calculated by using the following relation [10]

$$\bar{\varepsilon} = (2/\sqrt{3}) \ln (h/h_1) \quad (17)$$

in which  $h_1$  denotes original thickness of the specimen. The uniaxial flow stress (effective stress) is calculated using the expression [10]

$$\bar{\sigma} = (\sqrt{3}/2)(F/ab) \quad (18)$$

The disadvantages of plane-strain compression test are [11]

- The anvils must be kept exactly aligned under each other because even a small lateral shift will decrease the area under load.
- Along the edges of the dies, there is a stress concentration which may cause crack initiation at a strain for which no cracks would occur under an uniaxial load.

## Torsion Test

Because complications associated with necking (tension test) and barreling (compression test) are avoided, the torsion test can be used to obtain  $\bar{\sigma}$  -  $\bar{\epsilon}$  data at higher strains, often in excess  $\bar{\epsilon} = 2$ . Therefore, it is used when  $\bar{\sigma}$  -  $\bar{\epsilon}$  must be known for bulk forming operations such as extrusion, radial forging, or pilger rolling, in which very large strains are present.

In the torsion test, a hollow tube or solid bar is twisted at a constant rotational speed; the torque  $M$  and the number of rotations  $\theta$  (in radians) are measured.

For a *tubular* specimen (internal radius =  $r$ , wall thickness =  $t$ , and gage length =  $l$ ), the average shear stress  $\tau$  in the gage section is given by:

$$\tau = \frac{M}{2\pi r^2 t} \quad (19)$$

The shear strain  $\gamma$  is:

$$\gamma = \frac{r\theta}{l} \quad (20)$$

And the corresponding shear strain rate  $\dot{\gamma}$  is

$$\dot{\gamma} = \frac{r\dot{\theta}}{l} \quad (21)$$

For a *solid bar* of radius  $R$  and gage length  $l$ , the shear stress is given by the following relation [12]:

$$\tau = \frac{(3 + n^* + m^*)M}{2\pi R^3} \quad (22)$$

Here,  $n^*$  and  $m^*$  denote the instantaneous slopes of  $\log M$ -vs- $\log \theta$  and  $\log M$ -vs- $\log \dot{\theta}$  plots, respectively. In most cases  $n^* \sim n$ , the strain-hardening exponent, and  $m^* \sim m$ , the strain-rate-sensitivity exponent. The corresponding shear strain and shear strain rate are those pertaining to the outer surface of the specimen, i.e.,

$$\gamma = \frac{R\theta}{l} \quad (23)$$

$$\dot{\gamma} = \frac{R\dot{\theta}}{l} \quad (24)$$

Assuming that the material can be considered to be isotropic,  $\tau - \gamma$  results from the torsion test can be correlated to those from the uniform tension or compression tests using the following relations derived from the von Mises yield criterion:

$$\bar{\sigma} = \sqrt{3}\tau \quad (25)$$

and

$$\bar{\varepsilon} = \gamma / \sqrt{3} \quad (26)$$

## Split-Hopkinson Bar Test

Forming processes such as hot or cold rolling which are carried out at high rates of deformation necessitate flow stress data at high strain rates. For this purpose, the split Hopkinson pressure bar is used for compression tests (as well as tension or torsion tests) at high strain rates at room or elevated temperature.

A schematic illustration of the test apparatus is shown in Figure 13. The apparatus contains a striker, an incident bar, and a transmitted bar. Figure 13a shows the general elastic wave propagation in compressive test. In compression, when the striker bar impacts the incident bar, a compressive stress pulse is generated and travels through incident bar until it hits the specimen. At the bar/specimen interface part of the incident stress pulse is reflected due to material (impedance) mismatch. The transmitted pulse emitted from the specimen reaches the free end of transmitted bar and is reflected there as a tension pulse. The tensile stress pulse travels back through the transmitted bar, and upon reaching the specimen/transmitted bar interface, results in separation, thus ending the test. The stress, strain, and strain rate in the specimen are calculated in terms of strains recorded from the two strain gauges A and B.

In tension version of the test (Figure 13b), the specimen is attached to incident and transmitted bars. The compressive stress pulse generated in the incident bar travels along the specimen until it reaches the end of the transmitted bar. After reflection, the tensile stress pulse propagates through specimen to the incident bar. Strains recorded by strain gauges A and B are measured [13].

## Indentation Tests

Indentation tests are attractive for determining flow-stress data under the following conditions [14].

- The sample size is limited because of the process technology involved or when the number of materials to be tested is large.

- Testing of coated components. A number of engineering components are coated with different materials to improve their durability. Using indentation tests, flow stress behavior of coatings can be estimated by adjusting the indentation load.

At a given strain, the flow stress  $\bar{\sigma}$  and hardness value H are given by the relation [14]

$$H(\varepsilon) = C_f \bar{\sigma}(\varepsilon), \quad (27)$$

in which  $C_f$  is the constraint factor. The method for determining flow stress-strain relationship from static or dynamic hardness tests using the constraint factor approach is given in Reference 14. Flow curves can also be obtained from hardness measurements by continuously measuring the force and depth of indentation. However, this requires an extremely high degree of measurement accuracy [14].

## Effect of Deformation Heating on Flow Stress

The plastic work imposed during metalworking is dissipated by the formation of metallurgical defects (e.g., dislocations) and the generation of heat. The former usually accounts for 5-10 pct. of the work, while deformation heating accounts for 90-95 pct. of the work. Depending on the particular size of the workpiece, a greater or lesser amount of the deformation heat dissipates into the dies. For the sample sizes typically used to determine flow stress (e.g., ~12-mm diameter x 18-mm height cylinders for isothermal compression tests), a measurable fraction of the heat is retained in the workpiece for strain rates of the order of  $0.01 \text{ s}^{-1}$  or greater. For these strain rates, it becomes important to correct flow-stress data for the temperature rise associated with deformation heating.

The temperature increase  $\Delta T$  can be estimated from the following relation:

$$\Delta T \sim \frac{0.90\eta \int \bar{\sigma} d\varepsilon}{\rho_d c} \quad (28)$$

Here,  $\eta$  denotes the adiabaticity factor (=fraction of the deformation heat retained in the sample),  $c$  is the specific heat, and  $\rho_d$  is the density. The integral represents the area under the “uncorrected” true

stress-strain curve from a strain of zero to the strain for which the temperature rise is to be calculated. The adiabaticity factor for hot compression testing of small samples is equal to ~0.5, ~0.9, or ~1 for strain rates of 0.1, 1, and  $10\text{ s}^{-1}$  [15, 16].

The procedure for correcting flow curves for deformation heating comprises the following steps:

- (i) Calculate the temperature rise (Equation (28)) for a number of specific strain levels for each of several flow curves measured at different nominal test temperatures and a given strain rate.
- (ii) Construct plots of measured flow stress versus instantaneous temperature (equal to nominal test temperature +  $\Delta T$ ) for each of the given strains from step (i).
- (iii) Determine the value of  $d\bar{\sigma}/dT$  for a series of strains and nominal test temperatures from the stress-versus-temperature plots.
- (iv) Using these values of  $d\bar{\sigma}/dT$  and the calculated temperature rise, estimate what the isothermal flow stress would have been in the absence of deformation heating at a series of strains for each measured flow curve.

## Fitting of Flow Stress Data

Various analytical equations have been used to fit the flow stress data obtained from tension, compression, and torsion tests. The specific form of the equation usually depends on the test temperature (i.e., cold-working versus hot-working temperatures) and, at hot-working temperatures, on the strain rate. The definition of the temperature for cold versus hot working is not precise. However, the transition usually occurs at approximately one-half of the melting point on an absolute temperature scale. From a metallurgically standpoint, hot working is characterized by a *steady-state* flow stress beginning at modest strains (order of 0.25) due to dynamic recovery or by the occurrence of *discontinuous* dynamic recrystallization.

### Cold-Working Temperatures

A typical  $\bar{\sigma}$ - $\bar{\varepsilon}$  curve obtained at cold-working temperatures is shown in Figure 6b. Strain hardening is pronounced, but the strain-rate dependence is usually minimal. The flow stress  $\bar{\sigma}$  increases with increasing  $\bar{\varepsilon}$  and, for some materials, may eventually reach a saturation stress at very large true strains (usually  $\bar{\varepsilon} > 1$ ). Because of the parabolic shape of the flow curve at cold-working temperatures, true stress-strain data can often be fit by a power-law type of relation mentioned previously in this article, viz.,

$$\bar{\sigma} = K\bar{\epsilon}^n \quad (8)$$

in which  $K$  and  $n$  are material constants known as the strength coefficient and strain-hardening exponent, respectively. A log-log plot of experimental data can be used to determine whether Equation (8) provides a good fit. If so, the data fall on a straight line of slope equal to  $n$ , and the strength coefficient  $K$  is equal to the flow stress at a true strain of unity. Often at small strains, an experimentally determined curve may depart from linearity on the log-log plot. In this case, other values of  $n$  and  $K$  may be specified for different ranges of true strain. Typical values of  $n$  and  $K$  describing the flow-stress behavior of various metals at cold-working temperatures are given in Tables 1-3.

Other analytical expressions have been utilized to fit the true stress-strain curves for metals at cold-working temperatures. These include the following (in which  $a$ ,  $b$ , and  $c$  are material/fitting constants that differ in each equation):

$$\text{Ludwik Equation: } \bar{\sigma} = a + b(\bar{\epsilon})^c, \quad (29)$$

$$\text{Voce Equation: } \bar{\sigma} = a + [b - a] * [1 - \exp(-c\bar{\epsilon})] \quad (30)$$

$$\text{Swift Equation: } \bar{\sigma} = c(a + \bar{\epsilon})^n \quad (31)$$

The Ludwik equation approximates the stress-strain curves for annealed materials, but tends to underestimate the stress at low strains ( $<0.2$ ) and to overestimate the stress for high strains. For heavily prestrained materials,  $c \sim 1$ . The Voce and Swift equations tend to be used less frequently, partly because of their greater complexity.

### ***Hot-Working Temperatures***

At hot working temperatures,  $\bar{\sigma}$  increases with increasing  $\dot{\bar{\epsilon}}$  and with decreasing temperature  $T$ . Irrespective of strain rate, the flow curve generally exhibits a short strain-hardening transient followed by a peak stress. In materials whose principal dynamic restorative mechanism is dynamic recovery, subsequent deformation is characterized by a steady-state flow stress equal to the peak stress. In materials which undergo *discontinuous* dynamic recrystallization (characterized by the nucleation and growth of new, strain free grains during deformation), flow softening occurs following the peak stress until a steady-state microstructure and flow stress is achieved. These phenomena are described more extensively in the subsequent section dealing with Metallurgical Considerations at Hot-Working Temperatures.

In many engineering hot-working applications, a simple power-law equation is used to describe the flow stress as a function of strain rate:

$$\bar{\sigma} = C \dot{\epsilon}^m \quad (32)$$

Here,  $C$  is a constant (or a function of strain sometimes needed to describe the low-strain, strain-hardening dependence) and  $m$  is the strain-rate sensitivity exponent. A log-log plot of  $\bar{\sigma}$ - $\dot{\epsilon}$  data can be used to determine whether Equation (32) provides a good fit. If so, the data fall on a straight line of slope equal to  $m$ . Some typical  $C$  and  $m$  values for various metals are given in Tables 4-7 [17]. It has also been found that the dependence of the  $m$  value on homologous temperature (the ratio of the test temperature to the melting point on the absolute temperature scale) is similar for many metallic materials (Figure 14) [18].

## **Metallurgical Considerations at Hot-Working Temperatures**

The flow stress of a metallic material is closely coupled to its initial microstructure and how its microstructure evolves as a function of strain, strain rate, and temperature. Thus, the measured flow stress is actually the average *macroscopic* deformation resistance associated with a number of *micromechanical* processes such as the glide (slip) and climb of dislocations, dislocation annihilation, slip transfer across grain boundaries, dynamic recrystallization, dynamic grain growth/coarsening, etc. For this reason, a particular set of flow stress measurements is specific to the initial material and material condition for which it has been obtained.

Some of the important metallurgical factors that aid in the interpretation of flow curves at hot-working temperatures are summarized in this section. These include the influence of dynamic recovery and dynamic recrystallization on flow response and the effect of microstructural features (e.g., grain size, crystallographic texture, and second phases) on plastic flow.

### ***Deformation Mechanisms at Conventional Metalworking Strain Rates***

The key mechanisms that control microstructure evolution and plastic flow during hot (and to some extent cold) working at conventional metalworking strain rates ( $\dot{\epsilon} \geq 0.1 \text{ s}^{-1}$ ) are dynamic recovery and dynamic recrystallization [19, 20]. As the terms imply, dynamic recovery and recrystallization occur *during* hot working. As metals are worked, defects are generated in the crystal lattice. The most important defects are line defects known as dislocations. As deformation increases, the deformation resistance increases due to increasing dislocation content. However, the dislocation

density does not increase without limit because of the occurrence of dynamic recovery and dynamic recrystallization.

In high-stacking-fault-energy (SFE) metals (e.g., aluminum and its alloys, iron in the ferrite phase field, titanium alloys in the beta phase field), dynamic recovery (DRV) predominates. During such processes, individual dislocations or pairs of dislocations are annihilated because of the ease of climb (and the subsequent annihilation of dislocations of opposite sign) and the formation of cells and subgrains which act as sinks for moving (mobile) dislocations. Because subgrains are formed and destroyed continuously during hot working, hot deformed metals often contain a collection of *equiaxed* subgrains (with low misorientations across their boundaries) contained within *elongated* primary grains [20, 21]. Furthermore, the dynamic-recovery process leads to low stresses at high temperatures and thus cavity nucleation and growth are retarded, and ductility is high. The evolution of microstructure in high-SFE (and some low-SFE) materials worked at lower temperatures, such as those characteristic of cold-working, is similar. At these temperatures, subgrains may also form and serve as sinks for dislocations. However, the subgrains are more stable. Thus, as more dislocations are absorbed into their boundaries, increasing misorientations are developed, eventually giving rise to an equiaxed structure of high-angle boundaries. Such a mechanism forms the basis for grain refinement in so-called severe-plastic-deformation (SPD) processes. This mechanism of grain refinement is sometimes called *continuous* dynamic recrystallization (CDRX) because of the gradual nature of the formation of high angle boundaries with increasing strain.

In low-SFE materials (e.g., iron and steel in the austenite phase field, copper, nickel), dynamic recovery occurs at a lower rate under hot working conditions because mobile dislocations are dissociated, and therefore climb is difficult. This leads to somewhat higher densities of dislocations than in materials whose deformation is controlled by dynamic recovery. Furthermore, as the temperature is increased, the mobility of grain boundaries increases rapidly. Differences in dislocation density across the grain boundaries, coupled with high mobility, lead to the nucleation and growth of new, strain-free grains via a *discontinuous* dynamic recrystallization process (DDRX) [20, 22]. At large strains, a fully recrystallized structure is obtained. However, even at this stage, recrystallized grains are being further strained and thus undergo additional cycles of dynamic recrystallization. Nevertheless, a steady state is reached in which the rate of dislocation input due to the imposed deformation is balanced by dislocation annihilation due to the nucleation and growth of new grains (as

well as some dynamic recovery). Hence, although a nominally equiaxed grain structure is obtained at large strains, the distribution of stored energy is not uniform.

The presence of second phase particles may affect the evolution of microstructure during hot working of both high- and low-SFE materials. In high-SFE materials, particles may affect the homogeneity and magnitude of dislocation substructure that evolves. In low-SFE materials, particles may affect the evolution of substructure, serve as nucleation sites for dynamic recrystallization, as well as serve as obstacles to boundary migration during the recrystallization process.

### ***Flow Curves at Conventional Metalworking Strain Rates***

The stress-strain (flow) curves that are measured under conventional hot working conditions are a function of the predominant dynamic softening mechanism.

Flow Curves for Dynamic Recovery. As mentioned above, the hot-working response of high SFE metals is controlled by dynamic recovery. In such cases, dislocation generation is offset by dislocation annihilation due to recovery processes. The flow curve thus exhibits an initial stage of strain hardening followed by a steady-state (constant) flow stress. Typical flow curves for pure iron in the bcc phase field are shown in Figure 15 [23]. The magnitude of the steady state flow stress  $\bar{\sigma}_{ss}$  decreases with increasing temperature  $T$  and decreasing strain rate  $\dot{\varepsilon}$  typically according to a *phenomenological* (hyperbolic sine) relation as follows [19, 20]:

$$Z \equiv \dot{\varepsilon} \exp(Q/RT) = C' [\sinh((\alpha' \bar{\sigma}_{ss})]^{n_{drv}} \quad (33a)$$

in which  $Z$  denotes the Zener-Hollomon parameter,  $Q$  is an apparent activation energy,  $R$  is the gas constant, and  $C'$ ,  $\alpha'$ , and  $n_{drv}$  are constants. The constant  $n_{drv}$  is referred to as the stress exponent of the strain rate or simply the stress exponent. Equation (33a) reduces to two simpler forms depending on whether deformation is imposed at high temperature/low strain rate conditions (giving rise to low flow stresses) or at low temperature/high strain rate conditions (giving rise to high flow stress):

$$\text{Low stresses: } Z \equiv \dot{\varepsilon} \exp(Q/RT) \sim \bar{\sigma}_{ss}^{-n_{drv}} \quad (33b)$$

$$\text{High stresses: } Z \equiv \dot{\varepsilon} \exp(Q/RT) \sim \exp(\beta \bar{\sigma}_{ss}^{-n_{drv}}) \quad (33c)$$

The constants  $\alpha'$ ,  $\beta$ , and  $n_{drv}$  are related by  $\beta = \alpha' n_{drv}$ . Rearrangement of Equation (33b) yields an expression identical to Equation (32) in which the temperature dependence of the flow stress is incorporated into  $C$ , and the strain-rate sensitivity exponent  $m$  is equal to the inverse of the stress

exponent; i.e.,  $m = 1/n_{\text{drv}}$ . The loss of the power-law dependence of flow stress on strain rate at high stresses, i.e., Equation (33c) is termed power-law breakdown.

The activation energy  $Q$  in Equations (33a, b, c) can be determined from the slope of a plot of  $\log_{10} \bar{\sigma}$  versus  $1/T$  at fixed strain rate or  $\log_{10} \dot{\varepsilon}$  versus  $1/T$  at fixed stress, i.e.,

$$Q = \frac{2.3R}{m} \left. \frac{\partial \log \bar{\sigma}}{\partial (1/T)} \right|_{\dot{\varepsilon}} \quad (34a)$$

or,

$$Q = -2.3R \left. \frac{\partial \log \dot{\varepsilon}}{\partial (1/T)} \right|_{\bar{\sigma}} \quad (34b)$$

A more fundamental, *mechanistic* insight into the shape of the flow curve for cases involving dynamic recovery may be obtained by an analysis of the overall rate of change of (mobile) dislocation density  $\rho$  with strain  $\bar{\varepsilon}$ ,  $d\rho/d\bar{\varepsilon}$ , i.e.,

$$d\rho/d\bar{\varepsilon} = d\rho/d\bar{\varepsilon}|_{\text{storage}} - d\rho/d\bar{\varepsilon}|_{\text{recovery}} . \quad (35)$$

The specific functional form of the dislocation storage and annihilation terms in Equation (35) can be expressed as follows [24, 25]:

$$d\rho/d\bar{\varepsilon} = U - \Omega\rho . \quad (36)$$

In Equation (36),  $U$  denotes the rate of dislocation generation due to strain hardening, and  $\Omega$  is a factor describing the rate of dynamic recovery; the rate of recovery is also directly proportional to the instantaneous level of dislocation density  $\rho$ . At hot working temperatures,  $U$  is independent of strain rate and temperature to a first order [25]. Thus, the strain rate and temperature dependence of the rate of dislocation multiplication is determined principally by  $\Omega = \Omega(\dot{\varepsilon}, T)$ . An example of such a dependence for a low-carbon steel is shown in Figure 16a [25].

To a first order, the flow stress  $\bar{\sigma}$  under working conditions is given by the following expression:

$$\bar{\sigma} = \alpha G b \sqrt{\rho} , \quad (37)$$

in which  $\alpha$  denotes a constant whose magnitude is between 0.5 and 1.0,  $G$  is the shear modulus, and  $b$  is the length of the burgers (slip) vector. Inspection of Equations (36) and (37) reveals that the strain-rate and temperature dependence of the overall rate of hardening in the flow curve is largely determined by  $\Omega$ . The strain-hardening rate is frequently quantified in terms of plots of  $d\bar{\sigma}/d\bar{\varepsilon}$  ( $\equiv \theta$ ) as a function of  $\bar{\sigma}$ . Typical plots for low-carbon steel are shown in Figure 16b [25].

Equation (36) reveals that a steady state dislocation density  $\rho_{ss}$  is reached when  $U = \Omega\rho$ , or,

$$\rho_{ss} = U/\Omega , \quad (38)$$

The steady-state flow stress  $\bar{\sigma}_{ss}$  is thus given by the following relation:

$$\bar{\sigma}_{ss} = \alpha G b \sqrt{\rho_{ss}} = \alpha G b \sqrt{U/\Omega} . \quad (39)$$

Plastic-flow formulations such as Equations (35) – (39) form the basis of so-called *internal-state-variable* relations of the flow stress. This specific case utilizes a single state variable, the mobile dislocation density  $\rho$ .

There are a number of alternate approaches to the modeling of dynamic recovery under the broad framework of Equation (35). For example, Kocks [26] has shown that a linear dependence of strain-hardening rate ( $d\bar{\sigma}/d\bar{\epsilon}$ ) on stress ( $\bar{\sigma}$ ) is consistent with the following relation for  $d\rho/d\bar{\epsilon}$ :

$$d\rho/d\bar{\epsilon} = (k_1 \sqrt{\rho} - k_2 \rho)/b , \quad (40)$$

in which  $k_1$  and  $k_2$  are constants. Similarly, for a strain-hardening rate that varies linearly with  $1/\bar{\sigma}$ , Roberts [27] has shown that the following relation applies:

$$d\rho/d\bar{\epsilon} = k_3 - k_4 \sqrt{\rho} , \quad (41)$$

in which  $k_3$  and  $k_4$  are constants.

More information on internal-state-variable models is contained in the article “Constitutive/Internal State Variable Modeling of Flow Behavior of Crystalline Solids” in Volume 22A of the ASM Handbook.

Flow Curves for Discontinuous Dynamic Recrystallization. Flow curves for materials undergoing discontinuous dynamic recrystallization (DDRX) have shapes that are distinctively different from those that characterize materials which soften solely by dynamic recovery. Those for DDRX exhibit an initial strain hardening transient, a peak stress, flow softening, and, finally, a period of steady-state flow. Typical curves for two austenitic stainless steels are shown in Figure 17 [28].

Dynamic recrystallization typically initiates at a strain of approximately five-sixths of the strain corresponding to the peak stress. Because of this behavior, the peak stress for a material which undergoes dynamic recrystallization is *less* than that which would be developed if the material softened solely by dynamic recovery (Figure 18a). The strain at which DDRX initiates as well as the steady-state flow stress that would be developed in the absence of DDRX are readily determined from a plot of  $d\bar{\sigma}/d\bar{\epsilon}$  as a function of  $\bar{\sigma}$  (Figure 18b).

From a phenomenological standpoint, the strain at the peak stress  $\bar{\varepsilon}_p$  is usually found to depend on the initial grain size  $d_o$  and the Zener-Hollomon parameter  $Z$  per an expression of the following form [29-31]:

$$\bar{\varepsilon}_p = C'' d_o^{n_3} Z^{n_4}, \quad (42)$$

in which  $C''$ ,  $n_3$ , and  $n_4$  are material-specific constants. The activation energy specific to DDRX is used in the determination of  $Z$ .

The regime of steady-state flow in stress-strain curves for materials which undergo dynamic recrystallization may be smooth or exhibit an oscillatory behavior which dampens with increasing strain. Temperature-strain rate conditions for which the dynamically recrystallized grain size is less than one-half of the initial grain size show the former behavior. By contrast, those which give rise to grain-size coarsening or a reduction of less than one-half of the starting grain size exhibit the oscillatory behavior [32].

More information on the modeling of recrystallization is contained in the article “Models of Recrystallization” in Volume 22A of the ASM Handbook.

### ***Effect of Microstructural Scale on Flow Stress at Hot-Working Temperatures***

The effect of microstructural scale (grain size, thickness of lamellae, etc.) on the flow stress can at hot-working temperatures varies from relatively weak to very strong. By and large, the influence is very small or negligible when the scale of the primary microstructural feature is of the order of 10-20 microns or greater. Below this size, the effect increases as the scale decreases. Two important examples include the plastic flow of materials with a lamellar (colony) or acicular microstructure and the superplastic flow of metals with a very fine equiaxed grain structure.

For materials with a colony or acicular microstructure, such as two phase (alpha-beta) titanium alloys [33] and zirconium alloys [34], the thickness of the lamellae or lath-like features is typically less than or equal to a few microns. In these cases, dynamic recovery and the formation of subgrains is difficult. As such, flow curves exhibit a short strain-hardening transient, a peak stress, and then substantial flow softening over a wide range of strain rates (e.g.,  $0.001 - 10 \text{ s}^{-1}$ ) (Figure 19a). The observed flow softening has been ascribed to slip transmission across interphase boundaries, dynamic spheroidization, lamellar kinking, among other factors. For alpha-beta titanium alloys, such as Ti-6Al-4V, with a colony/acicular alpha microstructure, the peak stress  $\bar{\sigma}_p$  follows a Hall-Petch dependence on platelet thickness [33, 35], i.e.,

$$\bar{\sigma}_p = M_T (\tau_o + k_s \ell^{-1/2}), \quad (43)$$

in which  $M_T$  denotes the Taylor factor for the specific texture,  $\tau_o$  is the friction (lattice) stress,  $k_s$  is the Hall-Petch constant ('reduced' by a factor equal to  $M_T$ ), and  $\ell$  is the platelet thickness. The slope of the lines on Hall-Petch plots (Figure 19b) depend on strain rate. However, the overall magnitudes of the slope are comparable to that predicted by the classical Eshelby model [36]. The loss of the Hall-Petch contribution to the strength (the term  $M_T k_s \ell^{-1/2}$  in Equation (43)) has also been found to correlate to the level of flow softening observed in flow curves for Ti-6Al-4V with a colony/acyclic microstructure [33].

Metals with a moderate-to-coarse equiaxed grain size tend to exhibit a rate sensitivity ( $m$  value) which varies only slightly with strain rate in the conventional hot working regime ( $0.01 \leq \dot{\varepsilon} \leq 50 \text{ s}^{-1}$ ). By contrast, the  $m$  values of metals with an ultrafine, equiaxed grain size ( $d \leq 10 \mu\text{m}$ ) vary strongly with strain rate (Figure 20). For such materials, a modest rate sensitivity ( $m \sim 0.25$ ) is shown at both very low strain rates (the conventional creep regime, or Region I, in Figure 20) and moderate-to-high strain rates (the so-called power-law creep regime, or Region III, in Figure 20). At intermediate rates (typically  $0.0001 \leq \dot{\varepsilon} \leq 0.005 \text{ s}^{-1}$ ), or Region II,  $m$  values are very high ( $m \sim 0.4$  to 1), and superplastic behavior (tensile elongations of the order of 500 pct. or more) is obtained. Under superplastic conditions, the majority of the deformation occurs by grain boundary sliding (gbs) and grain rotation. The flow stress under superplastic conditions is controlled not by the grain-boundary sliding per se but by the kinetics of the micromechanical process by which stress concentrations developed at grain-boundary triple points (due to grain rotation) are relieved. These processes include climb-limited glide of dislocations in the vicinity of grain boundaries (i.e., mantle regions) or diffusional flow either through the grains or along the grain boundaries. The former explanation (climb-limited glide of dislocations), first proposed by Gifkins [37] and later extended by Ghosh [38], appears to be the most successful explanation of superplasticity.

A generalized constitutive relation of the following form is often capable of describing the relationship between the flow stress  $\bar{\sigma}$ , strain rate  $\dot{\varepsilon}$ , and grain size  $d$  of single-phase alloys during superplastic deformation [39, 40]:

$$\dot{\varepsilon} = \left( \frac{ADGb}{kT} \right) \left( \frac{\bar{\sigma}}{G} \right)^n \left( \frac{b}{d} \right)^p \quad (44)$$

In Equation (44),  $A$  is a constant (usually of the order of 10),  $D$  is a diffusion parameter,  $k$  is Boltzmann's constant,  $T$  is absolute temperature,  $G$  is the shear modulus,  $b$  is the length of the Burgers vector,  $n$  is the stress exponent of the strain rate ( $=1/m$ ), and  $p$  is the grain size exponent of the strain rate. For superplastic flow characterized by gbs accommodated by climb/glide of dislocations,  $n \sim 2$  and  $p \sim 2$ . For gbs accommodated by diffusional flow,  $n \sim 1$  and  $p \sim 2$  or 3, depending on whether bulk (lattice) or boundary diffusion predominates, respectively.

The extension of the phenomenological relation between  $\dot{\varepsilon}$ ,  $\bar{\sigma}$ ,  $T$ , and  $d$  expressed by Equation (44) to two- (or multi-) phase alloys is not obvious. This is because an ambiguity arises as to which phase the values of  $D$ ,  $G$ ,  $\Omega$ ,  $d$ , and  $b$  relate. For example, for fine, equiaxed two-phase titanium alloys, hard alpha phase particles are surrounded by much softer beta-phase grains. In this instance, the alpha phase acts like the core (which deforms relatively little) and the beta phase like the mantle (which deforms to accommodate stress concentrations) in the Gifkins core-mantle model [37, 41]. The alpha particle size is thus taken to be  $d$ , and all of the other quantities pertain to the beta phase [41]. The applicability of this model for ultrafine Ti-6Al-4V deformed under superplastic conditions is shown in Figure 21a. The data in this figure have been plotted per Equation (44) rearranged to express  $AD$  as a function of  $1/T$  and the measured/imposed values of  $\bar{\sigma}$ ,  $\dot{\varepsilon}$ , etc. The plot also includes a line indicating the inverse temperature dependence of the diffusivity of vanadium solute in beta titanium. The similarity of the slope of this line and the trend line for the plastic flow measurements indicates an identical activation energy for the two processes. The fact that the plastic flow trend line lies above the diffusivity line by approximately one order of magnitude suggests that  $A \sim 10$ .

For materials which undergo grain growth or coarsening during superplastic flow, the value of  $d$  in Equation (44) increases with strain and must be taken into account when interpreting flow response. As an example, constant strain rate flow curves for the superplastic deformation of Ti-6Al-4V (used in part to derive Figure 21a) are shown in Figure 21b. The observed flow hardening is a result of the dynamic coarsening of the alpha particles [41, 42].

### ***Effect of Crystallographic Texture on Flow Stress***

Crystallographic texture, or the preferred orientation of the grains comprising a polycrystalline aggregate, can also have a major effect on the flow stress at hot- (and cold-) working temperatures. The influence is greatest for metals with low-symmetry crystal structures and metals of any crystal structure having a very strong texture.

Single-phase alpha and alpha-beta titanium alloys can exhibit stress-strain curves which vary noticeable with test direction as a result of a strong texture of the hcp alpha phase. For example, Figure 22a shows stress-strain curves measured in compression on samples cut from the rolling (“L”), long transverse (“T”), 45 degree, and short transverse/thickness (ST) directions in a textured plate of Ti-6Al-4V with a colony alpha microstructure [43]. Focusing on the peak stress, the plate was strongest along the rolling direction and weakest along the 45 degree direction in the plane. These trends correlated with the texture quantified in terms of inverse pole figures (Figure 22b). Basal poles were preferentially aligned with the L direction thus forcing the activation of the strong  $\langle c+a \rangle$  slip system in the hcp alpha lamellae. Similarly, prism poles were preferentially aligned with the 45 degree direction, thereby favoring the activation of the complementary (softer) prism  $\langle a \rangle$  systems.

The presence of a strong crystallographic texture even in a metal with a high-symmetry crystal structure (e.g., cubic) can also lead to flow curves which exhibit a directionality with test direction. For example, cast ingots of fcc metals typically have strong 100 fiber textures associated with the development of coarse columnar grains during solidification. When tested parallel or perpendicular to the columnar-grain/  $\langle 100 \rangle$ -fiber direction, the plastic-flow response will be different, as shown in the results for a production-scale Waspaloy ingot (Figure 23) [44]. Samples compressed transverse to the fiber-texture axis showed a peak stress following by flow softening, a behavior typical of a material undergoing discontinuous dynamic recrystallization. By contrast, the stress-strain curves from tests parallel to the fiber axis showed a lower peak stress followed by nearly steady state flow. These differences can be explained in terms of the evolution of the Taylor factor [44]. In the as-cast condition, the transverse samples had a higher Taylor factor than the axial samples and thus a higher peak stress. The Taylor factor after recrystallization of the transverse samples was similar to that initially, thus leading to the typical flow curve for material undergoing dynamic recrystallization. On the other hand, the Taylor factor of the axial samples increased during deformation due to recrystallization, thereby leading to an increment of texture hardening that counterbalanced the flow softening due to dynamic recrystallization.

### ***Effect of Second Phases on Flow Stress***

The flow stress of materials comprising two (or more) equiaxed phases (each of whose size is greater than or equal to  $\sim 10 \mu\text{m}$ ) is usually a complex function of the specific volume fraction and individual flow stress of each constituent. In particular, the activation energy of the alloy (determined

per Equation (34)) is often found to be a function of the volume fraction and activation energy of each, and thus exhibits a complex dependence on temperature.

Isostress, isostrain, and self-consistent modeling approaches have been used to understand the flow behavior of two-phase materials [45]. The self-consistent analysis appears to be the best, as demonstrated by its application for alpha-beta titanium alloys [46]. In brief, the analysis assumes (i) the flow behavior of each of the two individual phases can be described by a power-law relation of the form of Equation (32), (ii) the m value is the same for both phases, (iii) the strength coefficients of the two phases,  $C_1$  and  $C_2$ , are different. The analysis yields the overall strength coefficient of the alloy ( $C_{\text{alloy}}$ ) as a function of the volume fraction of the harder phase  $f_1$  and the ratio  $C_1/C_2$  and thus the alloy constitutive equation  $\bar{\sigma} = C_{\text{alloy}} \dot{\varepsilon}^m$ . Parametric results for  $m = 0.23$  are shown in Figure 24 [46]. Results for  $m = 0.15$  and  $m = 0.30$  (which typically span those commonly found during hot working) are similar.

The self-consistent analysis is also useful in quantifying the effect of temperature history on the flow stress of two-phase alloys [46, 47]. This is especially important for conventional metalworking and high strain rate processes in which die chill or deformation heating, respectively, gives rise to large temperature transients. The non-equilibrium microstructure developed during such processes (which can be quite different from that in typical isothermal compression, tension, and torsion tests) is quantified by diffusion models and coupled with the self-consistent analysis to predict flow stress.

More information on the application of the self-consistent method of modeling plastic flow and texture evolution is contained in the article “Modeling and Simulation of Texture Evolution during the Thermomechanical Processing of Titanium Alloys” in Volume 22A of the ASM Handbook.

**Acknowledgements-** Portions of this article were excerpted from (1) Shirgaokar, M., “Flow Stress and Forgeability,” in Altan, T., Ngaile, G., Shen, G., *Cold and Hot Forging: Fundamentals and Applications*, ASM International, Materials Park, OH, 2004, Chapter 4 and (2) Semiatin, S.L., “Evolution of Microstructure during Hot Working,” *Handbook of Workability and Process Design*, Dieter, G.E., Kuhn, H.A., and Semiatin, S.L., eds., ASM International, Materials Park, OH, 2003, p. 35.

## REFERENCES

1. Altan, T., Ngaile, G., Shen, G., *Cold and Hot Forging: Fundamentals and Applications*, ASM International, Materials Park, OH, 2004, chapter 4.
2. Thomsen, E.G., Yang, C.T., Kobayashi, S., *Mechanics of Plastic Deformation in Metal Processing*, MacMillan Company, New York, 1965.
3. Bridgman, P.W., *Studies in Large Plastic Flow and Fracture*, McGraw-Hill, New York, 1952.
4. Dahl, C., Vazquez, V., Altan, T., "Determination of Flow Stress of 1524 Steel at Room Temperature using the Compression Test," Report ERC/NSM-99-R-22, Engineering Research Center for Net Shape Manufacturing, The Ohio State University, Columbus, OH, 1999.
5. Lee, C.H., Altan, T., "Influence of Flow Stress and Friction upon Metal Flow in Upset Forging of Rings and Cylinders," *Trans. ASME, J. Eng. Ind.*, 1972, vol. 94, p. 775.
6. Douglas, J.R., Altan, T., "Flow Stress Determination of Metals at Forging Rates and Temperatures," *Trans. ASME, J. Eng. Ind.*, 1975, vol. 97, p. 66.
7. Altan, T., Oh, S.-I., and Gegel, H.L., *Metals Forming: Fundamentals and Applications*, ASM International, Materials Park, OH, 1983.
8. Watts, A.B., Ford, H., "On the Basic Yield Stress Curve for a Metal," *Proc. Inst. Mech. Eng.*, 1955, vol 169, p.1141.
9. Vollmer, J., "Measurement of Flow Stress of Metallic Materials Mainly for High Strains and High Strain Rates," Thesis, TU Hannover, 1969. (in German)
10. Totten, G.E., Funatani, K., Xie, L., "Handbook of Metallurgical Process Design", CRC press, 2004.
11. Pohlandt, K., "Materials Testing for the Metal Forming Industry," 1989.
12. Fields, D.S., Backofen, W.A., "Determination of Strain-Hardening Characteristics by Torsion Testing," *Proc. ASTM*, 1957, vol. 57, p. 1259.
13. Lee, O.S., Kim, S.M., "Dynamic Material Property Characterization Using Split Hopkinson Pressure Bar (SHPB) Technique," *Nuclear Engineering and Design*, 2003, vol. 226, p. 119.
14. Sundararajan, G., Tirupataiah, Y., "The Hardness-Flow Stress Correlation in Metallic Materials," *Bull.Mater.Sci.*, 1994, vol.17, p. 747.
15. Oh, S.I., Semiatin, S.L., Jonas, J.J., "An Analysis of the Isothermal Hot Compression Test," *Metall. Trans. A*, 1992, vol. 23A, p. 963.
16. Goetz, R.L., Semiatin, S.L., "The Adiabatic Correction Factor for Deformation Heating during the Uniaxial Compression Test," *J. Mater. Eng.'g. Perf.*, 2001, vol. 10, p. 710.

17. Altan, T., Boulger, F.W., "Flow Stress of Metals and Its Application in Metal Forming Analyses," *Trans. ASME, J. Eng. Ind.*, 1973, vol. 95, p. 1009.
18. Montheillet, F., Jonas, J.J., "Temperature Dependence of the Rate Sensitivity and its Effect on the Activation Energy for High-Temperature Flow," *Metall. Mater. Trans. A*, 1996, vol. 27A, p. 3346.
19. Humphreys, F.J., Hatherly, M., *Recrystallization and Related Phenomena*, Elsevier, Oxford, U.K., 1995.
20. Jonas, J.J., McQueen, H.J., "Recovery and Recrystallization during High Temperature Deformation," in *Treatise on Materials Science and Technology*, edited by R.J. Arsenault, Academic Press, New York, 1975, p. 394.
21. McQueen, H.J., Hockett, J.E., "Microstructures of Aluminum Compressed at Various Rates and Temperatures," *Metall. Trans.*, 1970, vol. 1, p. 2997.
22. Doherty, R.D., Hughes, D.A., Humphreys, F.J., Jonas, J.J., Juul Jensen, D., Kassner, M.E., King, W.E., McNelley, T.R., McQueen, H.J., Rollett, A.D., "Current Issues in Recrystallization: A Review," *Mater. Sci. Eng. A*, 1997, vol. A238, p. 219.
23. Immarigeon, J.-P.A., Jonas, J.J., "The Deformation of Armco Iron and Silicon Steel in the Vicinity of the Curie Temperature," *Acta Metall.*, 1974, vol. 22, p. 1235.
24. Yoshie, A., Mirikawa, H., Onoe, Y., "Formulation of Static Recrystallization of Austenite in Hot Rolling Process of Steel Plate," *Trans. ISIJ*, 1987, vol. 27, p. 425.
25. Laasraoui, A., Jonas, J.J., "Prediction of Steel Flow Stresses at High Temperatures and Strain Rates," *Metall. Trans. A*, 1991, vol. 22A, p. 1545.
26. Kocks, U.F., "Laws for Work Hardening and Low-Temperature Creep," *Trans. ASME, J. Eng. Mater. Techn.*, 1976, vol. 98, p. 76.
27. Roberts, W., "Dynamic Changes That Occur During Hot Working and Their Significance Regarding Microstructural Development and Hot Workability," in *Deformation, Processing, and Structure*, edited by G. Krauss, ASM, Metals Park, OH, 1984, p. 109.
28. Ryan, H.D., McQueen, H.J., "Comparative Hot Working Characteristics of 304, 316, and 317 Steels, Both Cast and Worked," in *Inter. Conf. on New Developments in Stainless Steel Technology*, edited by R.A. Lula, ASM, Metals Park, OH, 1985, p. 293.
29. Sellars, C.M., "Modeling Microstructure Evolution," *Mater. Sci. Techn.*, 1990, vol. 6, p. 1072.

30. Devadas, C., Samarasekara, I.V., Hawbolt, E.B., "Thermal and Metallurgical State of Steel Strip during Hot Rolling," *Metall. Trans. A*, 1991, vol. 22A, p. 335.
31. Shen, G., Semiatin, S.L., Shrivpuri, R., "Modeling Microstructural Development during the Forging of Waspaloy," *Metall. Mater. Trans. A*, 1995, vol. 26A, p. 1795.
32. Sakai, T., Jonas, J.J., "Dynamic Recrystallization: Mechanical and Microstructural Considerations," *Acta Metall.*, 1984, vol. 32, p. 189.
33. Semiatin, S.L., Bieler, T.R., "The Effect of Alpha Platelet Thickness on Plastic Flow during Hot Working of Ti-6Al-4V with a Transformed Microstructure," *Acta Mater.*, 2001, vol. 49, p. 3565.
34. Abson, D.J., Jonas, J.J., "Hot Compression Behavior of Thermomechanically Processed Alpha Zirconium," *Metals Techn.*, 1977, vol. 4, p. 462.
35. Armstrong, R., Codd, I., Douthwaite, R.M., Petch, N.J., "The Plastic Deformation of Polycrystalline Aggregates," *Phil. Mag.*, 1962, vol. 7, p. 45.
36. Eshelby, J.D., *Phys. Stat. Solidi*, "The Distribution of Dislocations in an Elliptical Glide Zone," 1963, vol. 3, p. 2057.
37. Gifkins, R.C., "Grain-Boundary Sliding and Its Accommodation during Creep and Superplasticity," *Metall. Trans. A*, 1976, vol. 7A, p. 1225.
38. Ghosh, A.K. in: *Metalworking: Bulk Forming*, Volume 14A, ASM Handbook, Tenth Edition, S.L. Semiatin, ed., ASM International, Materials Park, OH, 2005, p. 563.
39. Bird, J.E., Mukherjee, A.K., Dorn, J.E. in: *Quantitative Relation Between Microstructure and Properties*, D.G. Brandon and A. Rosen, eds., Israel Universities Press, Jerusalem, Israel, 1969, p. 255.
40. Langdon, T.G., "Grain-Boundary Sliding Revisited: Developments in Sliding over Four Decades," *J. Mater. Sci.*, 2006, vol. 41, p. 597.
41. Sargent, G.A., Zane, A.P., Fagin, P.N., Ghosh, A.K., Semiatin, S.L., "Low-Temperature Coarsening and Plastic Flow Behavior of an Alpha/Beta Titanium Billet Material with an Ultrafine Microstructure," *Metall. Mater. Trans. A*, 2008, vol. 39A, p. 2949.
42. Semiatin, S.L., Corbett, M.W., Fagin, P.N., Salishchev, G.A., Lee, C.S., "Dynamic-Coarsening Behavior of an Alpha/Beta Titanium Alloy," *Metall. Mater. Trans A*, 2006, vol. 37A, p. 1125.

43. Semiatin, S.L., Bieler, T.R., "Effect of Texture and Slip Mode on the Anisotropy of Plastic Flow and Flow Softening during Hot Working of Ti-6Al-4V," *Metall. Mater. Trans. A*, 2001, vol. 32<sup>a</sup>, p. 1787.
44. Semiatin, S.L., Weaver, D.S., Fagin, P.N., Glavicic, M.G., Goetz, R.L., Frey, N.D., Kramb, R.C., and Antony, M.M., "Deformation and Recrystallization Behavior during Hot Working of a Coarse-Grain, Nickel-Base Superalloy Ingot Material," *Metall. Mater. Trans. A*, 2004, vol. 35A, p. 679.
45. Briottet, L., Jonas, J.J., Montheillet, F., "A Mechanical Interpretation of the Activation Energy of High-Temperature Deformation in Two-Phase Materials," *Acta Mater.*, 1996, vol. 44, p. 1665.
46. Semiatin, S.L., Montheillet, F., Shen, G., Jonas, J.J., "Self-Consistent Modeling of the Flow Behavior of Wrought Alpha/Beta Titanium Alloys under Isothermal and Nonisothermal Hot-Working Conditions," *Metall. Mater. Trans. A*, 2002, vol. 33A, p. 2719.
47. Shen, G., Semiatin, S.L., Kropp, E., Altan, T., "A Technique to Compensate for Temperature-History Effects in the Simulation of Nonisothermal Forging Processes," *J. Mater. Proc Techn.*, 1992, vol. 33, p. 125.

### **Further Reading**

- Altan, T., Semiatin, S.L., Lahoti, G.D., "Determination of Flow Stress Data for Practical Metal Forming Analysis," *Ann. CIRP*, Vol 30 (No. 1), 1981, p 129.
- Lahoti, G.D., Altan, T., "Prediction of Temperature Distributions in Axisymmetric Compression and Torsion," *J. Eng. Mater. Technol.*, April 1975, p 113.

## Figure Captions

**Figure 1.** Data from the uniaxial tension test: (a) Engineering stress-strain curve, (b) true stress-strain curve, and (c) schematic illustration of dimensional changes during the test. [2]

**Figure 2.** Determination of the strain at the onset of necking during the tension test. [2]

**Figure 3.** Axial stress distribution at the symmetry plane of a necked portion of a tension specimen. [2, 3]

**Figure 4.** Compression test specimen: (a) View of specimen, showing lubricated shallow grooves on the ends and (b) shape of the specimen before and after the test.

**Figure 5.** Typical specimen designs for the compression testing of cylinders: (a) Sample with spiral grooves or (b) Rastegaev specimen. [4]

**Figure 6.** Room-temperature data for annealed aluminum alloy 1100: (a) Load-displacement curve from a cylinder-compression test and (b) true stress-true strain (flow) curve results from both cylinder compression and ring compression. [5]

**Figure 7.** Press setup and sample tooling design used for the hot compression of cylinders and rings.

**Figure 8.** Compression samples before and after hot deformation. (Left to right: AISI 1018 steel, nickel alloy 718, Ti-6Al-4V)

**Figure 9.** Flow curves for (a) Type 403 stainless steel at 1800, 1950, and 2050°F (980, 1065, and 1120°C) and (b) Waspaloy at 1950, 2050, and 2100°F (1065, 1120, and 1150°C). The tests were conducted in a mechanical press in which the strain rate was not constant. [6]

**Figure 10.** The ring test: (a) Schematic of metal flow and (b) example rings upset to various reductions in height.

**Figure 11.** Calibration curves for isothermal compression of rings having initial OD: ID: thickness ratios of (a) 6:3:2, (b) 6:3:1, or (c) 6:3:0.5. [7]

**Figure 12.** Schematic illustration of the plane-strain compression test. [11]

**Figure 13.** Schematic diagram of specimen design and stress-wave propagation for (a) compressive and (b) tensile Hopkinson-bar tests. [13]

**Figure 14.** Comparison of measurements (data points) of the strain-rate-sensitivity exponent ( $m$ ) as a function of the homologous temperature (fraction of the melting point) for various materials and an analytical model (solid line). [18]

**Figure 15.** Flow curves for Armco iron deformed under hot-working conditions in the ferrite-phase field. [23]

**Figure 16.** Characterization of the flow behavior of a low carbon-steel under hot working conditions: (a)  $\Omega$  as a function of temperature and strain rate and (b) the overall hardening rate  $\theta = d\bar{\sigma} / d\bar{\varepsilon}$  as a function of stress  $\bar{\sigma}$  at a strain rate of  $2 \text{ s}^{-1}$  and various temperatures.[25]

**Figure 17.** Flow curves for 316 and 317 stainless steels deformed under hot-working conditions. [28]

**Figure 18.** Schematic illustration of work hardening behavior for a material undergoing dynamic recrystallization at hot-working temperatures: (a) stress-strain curve and (b) corresponding plot of  $d\bar{\sigma} / d\bar{\varepsilon}$  as a function of stress  $\bar{\sigma}$ .

**Figure 19.** Effect of alpha-platelet thickness on plastic flow of Ti-6Al-4V (with a lamellar/acicular microstructure) at 900°C: (a) Flow curves and (b) Hall-Petch plot for the peak flow stress,  $\bar{\sigma}_p$  [33].

**Figure 20.** Schematic illustration of the variation of flow stress with strain rate (on a log-log basis) for a fine-grain material which exhibits superplastic flow.

**Figure 21.** Superplastic flow of ultrafine Ti-6Al-4V: (a) Plot illustrating applicability of the generalized constitutive relation (Equation (41)) and (b) stress-strain data in the superplastic regime indicative of flow hardening due to dynamic coarsening [41].

**Figure 22.** Plastic flow behavior of textured plate of Ti-6Al-4V with a colony- (lamellar-) alpha microstructure: (a) Stress-strain curves of samples oriented along different directions in the plate and (b) the corresponding inverse pole figure for each compression-test direction [43].

**Figure 23.** Stress-strain curves from compression tests parallel (“axial”) or perpendicular (“transverse”) to the columnar-grain/<100>-fiber direction of a cast-and-homogenized Waspaloy ingot [44].

**Figure 24.** Predictions from a self-consistent model of the dependence of the strength coefficient of a two-phase alloy ( $C_{\text{alloy}}$ ) on the ratio of the strength coefficients of the two phases ( $C_1/C_2$ ) and the volume fraction of the harder phase ( $f_1$ ), assuming  $m_1 = m_2 = 0.23$  [46].

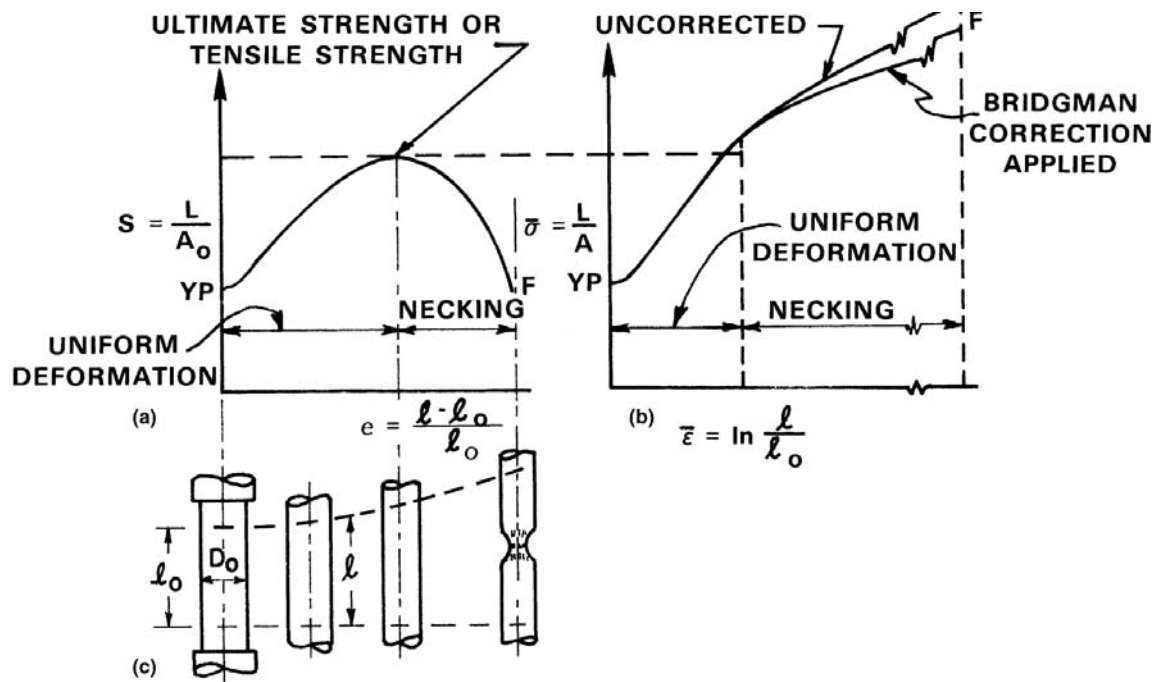


**Figure 1**

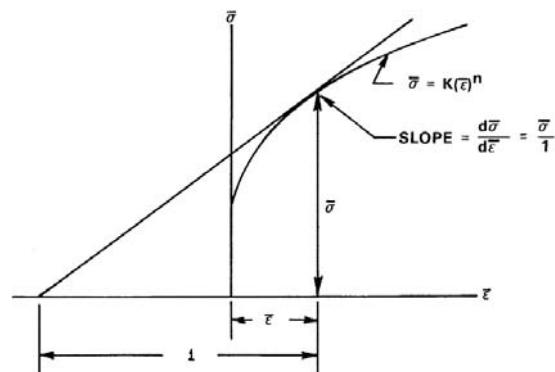


**Figure 2**

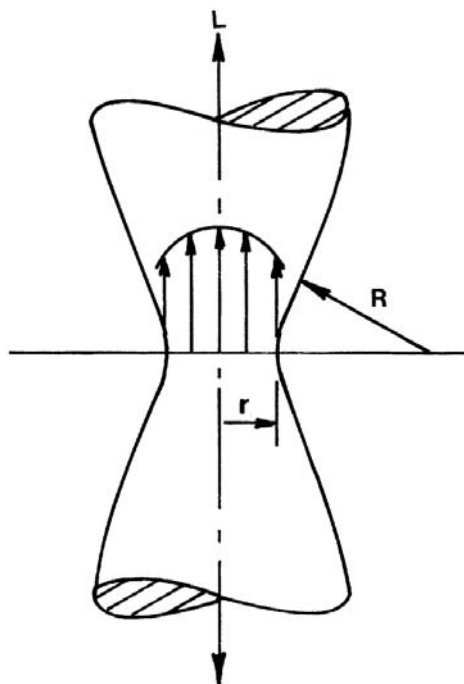


**Figure 3**

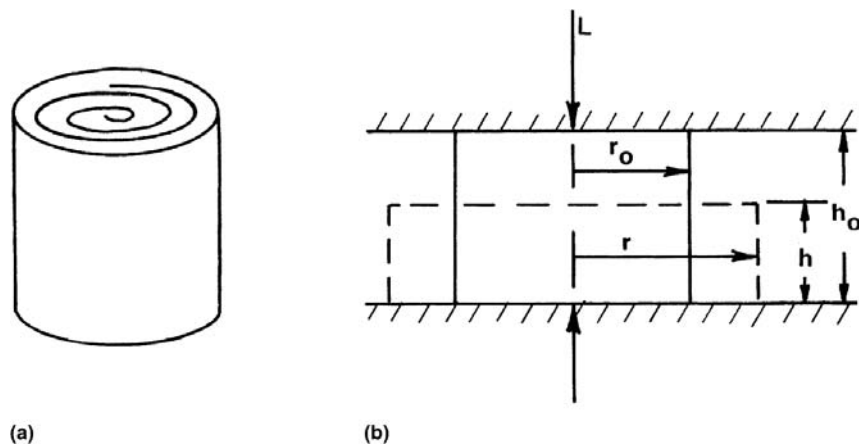


**Figure 4**

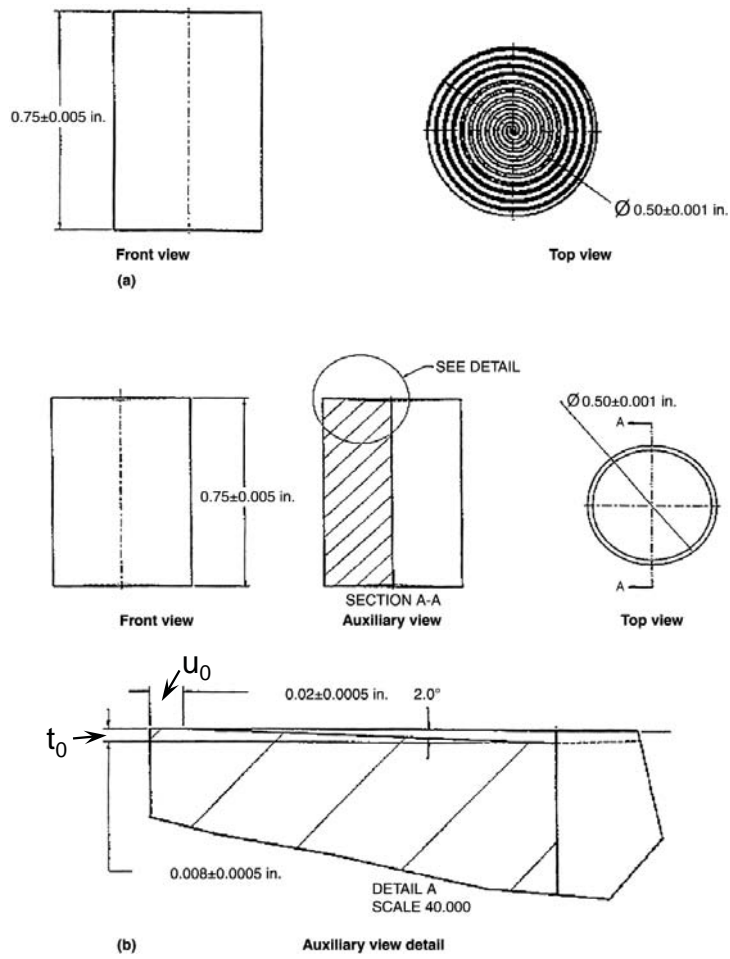


**Figure 5**

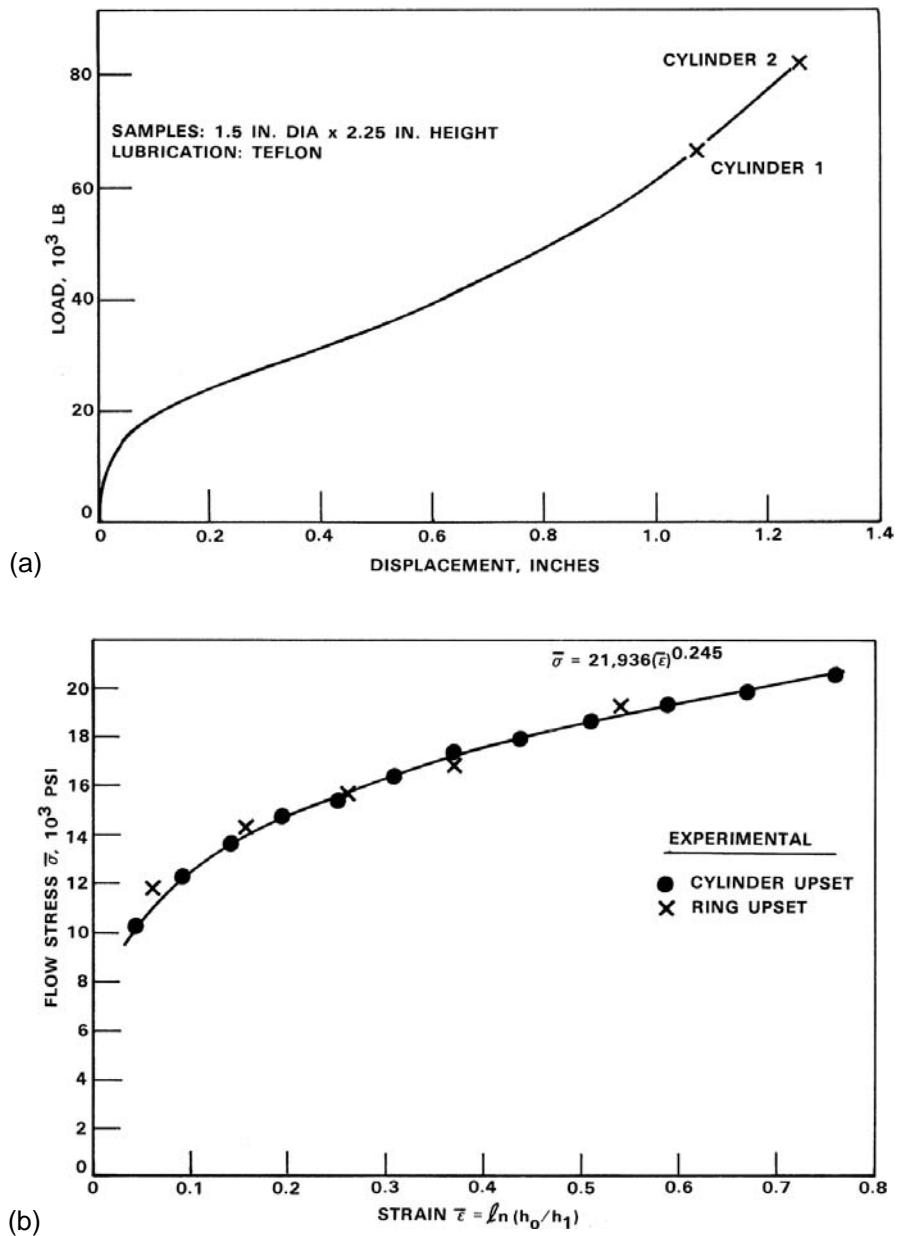
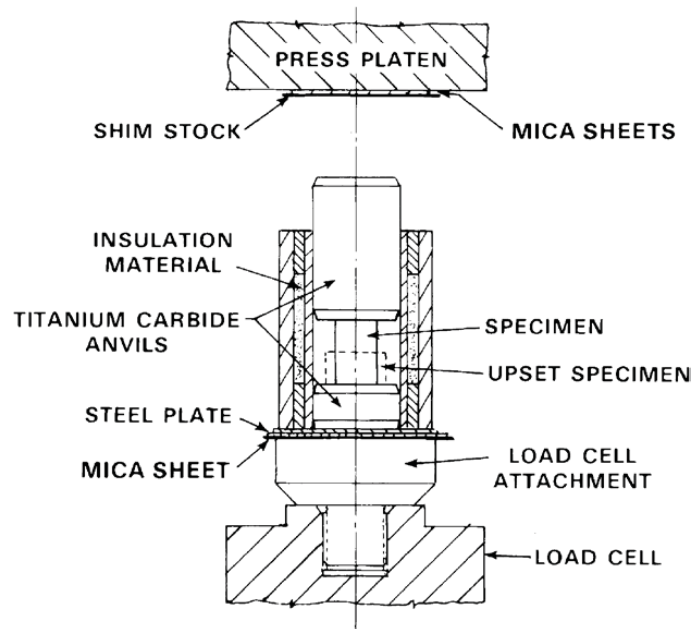
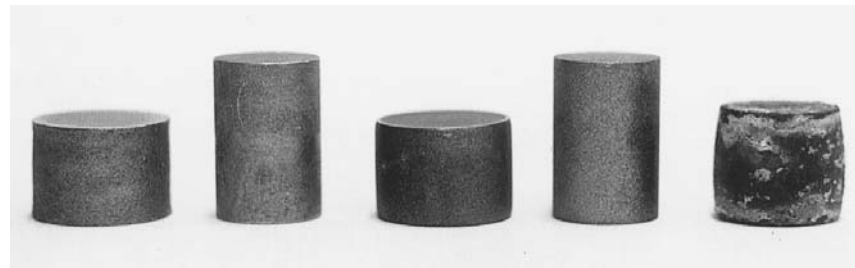


Figure 6



**Figure 7**



**Figure 8**

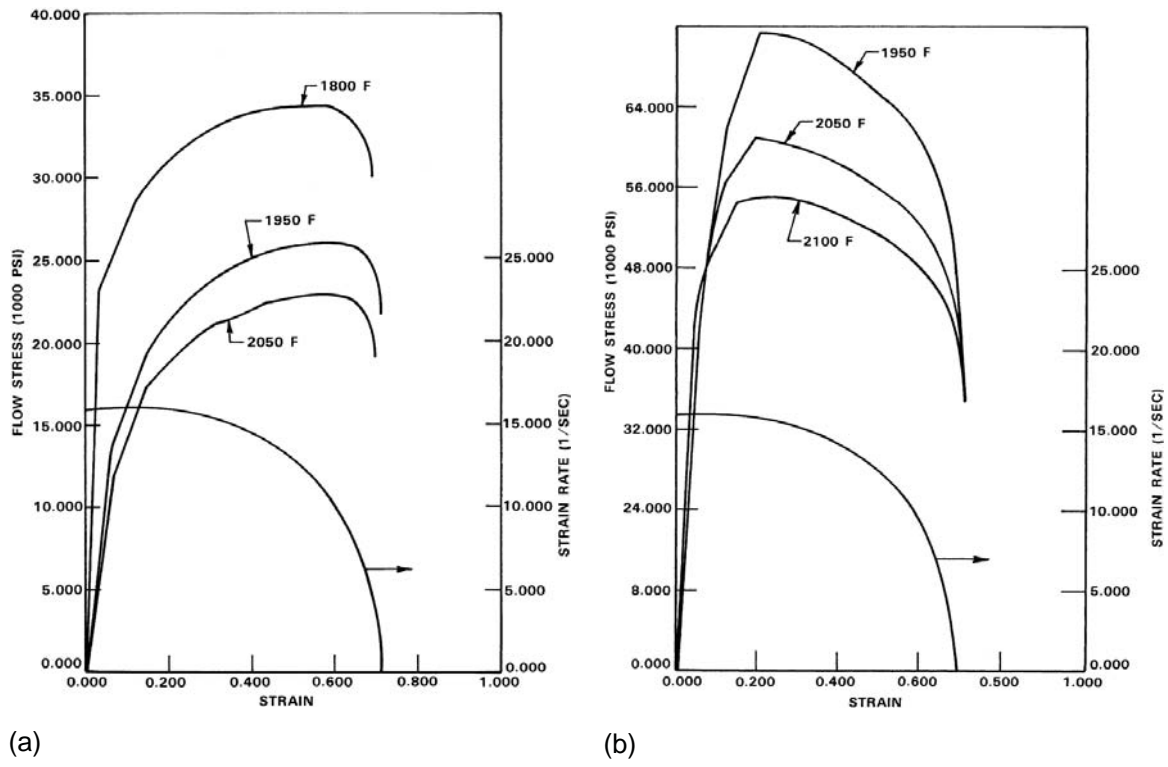
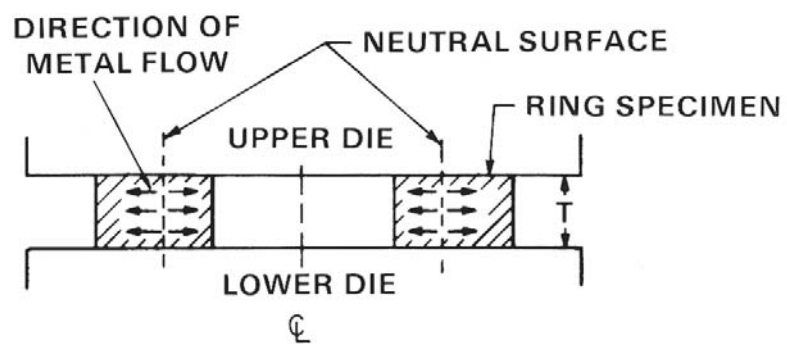
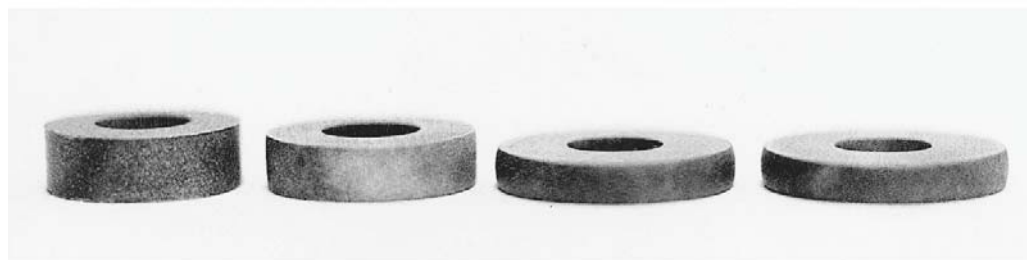


**Figure 9**



(a)



(b)

**Figure 10**

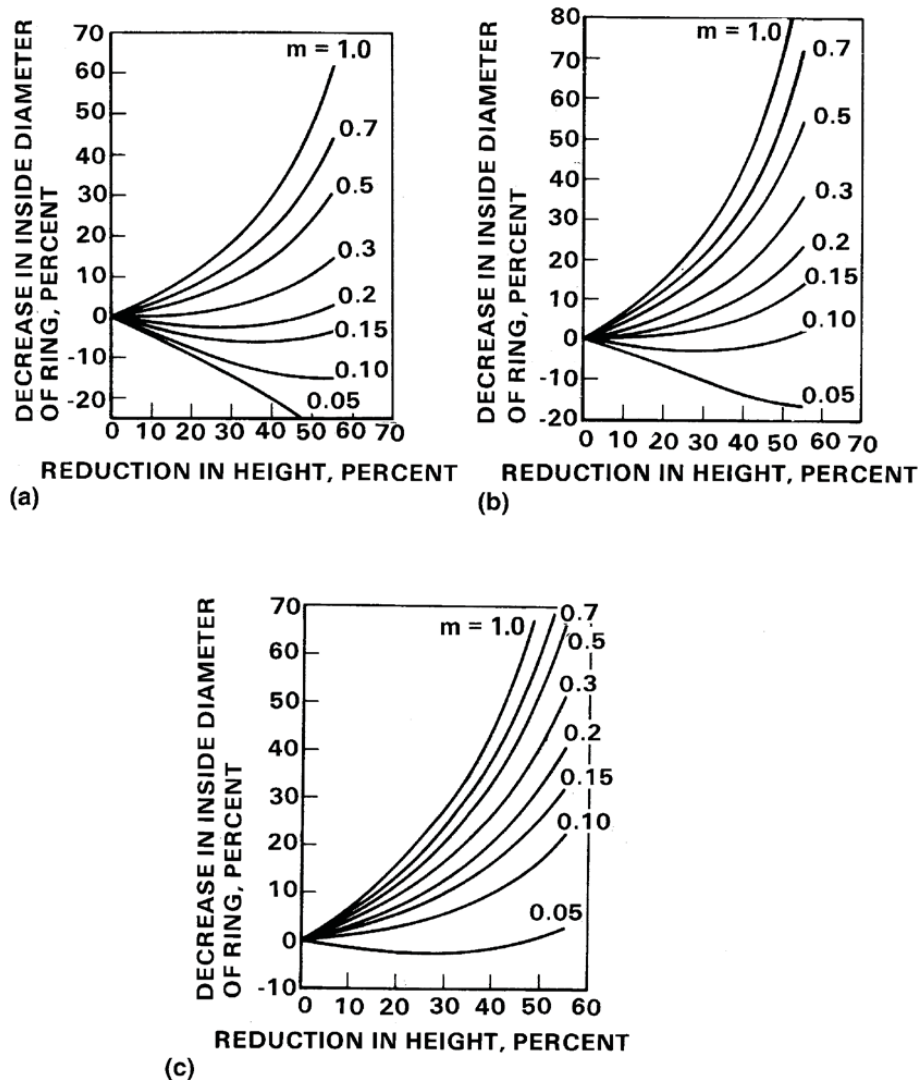


**Figure 11**

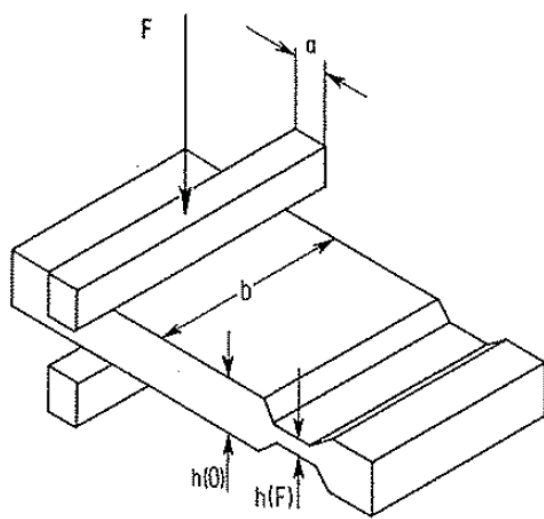


**Figure 12**

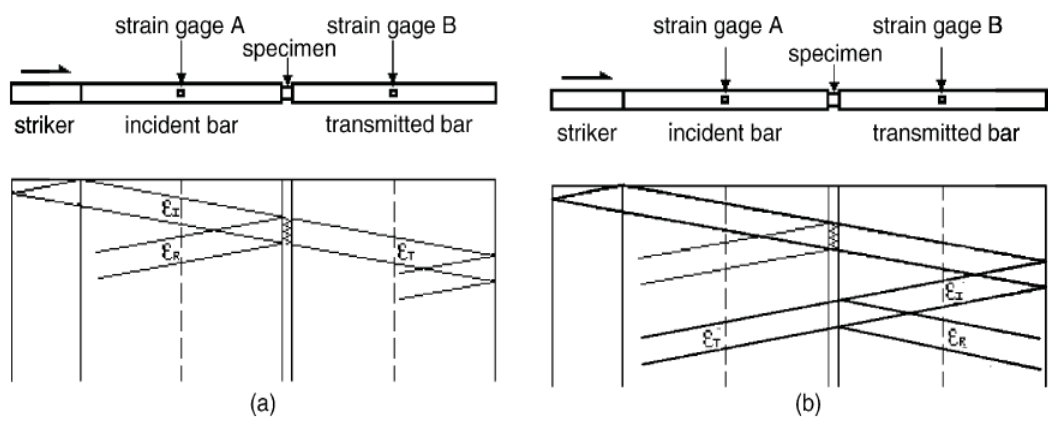


**Figure 13**

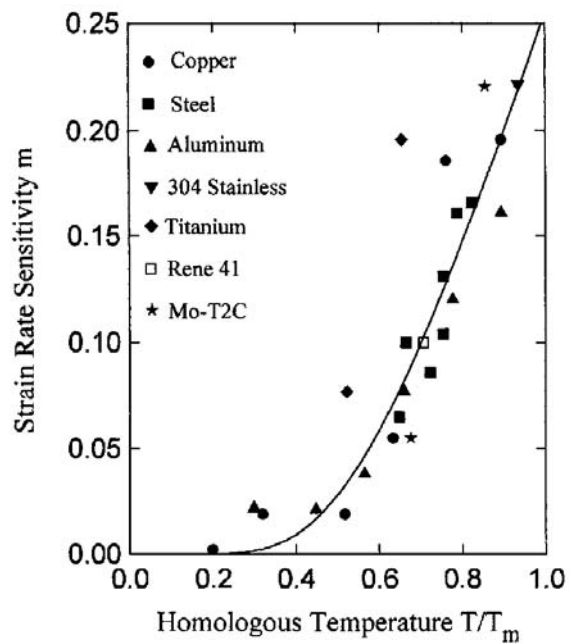


**Figure 14**

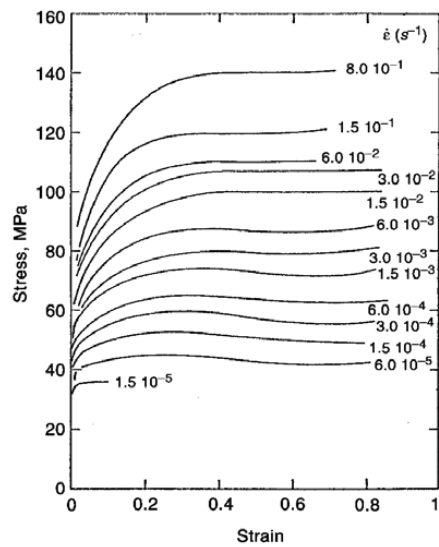


**Figure 15**

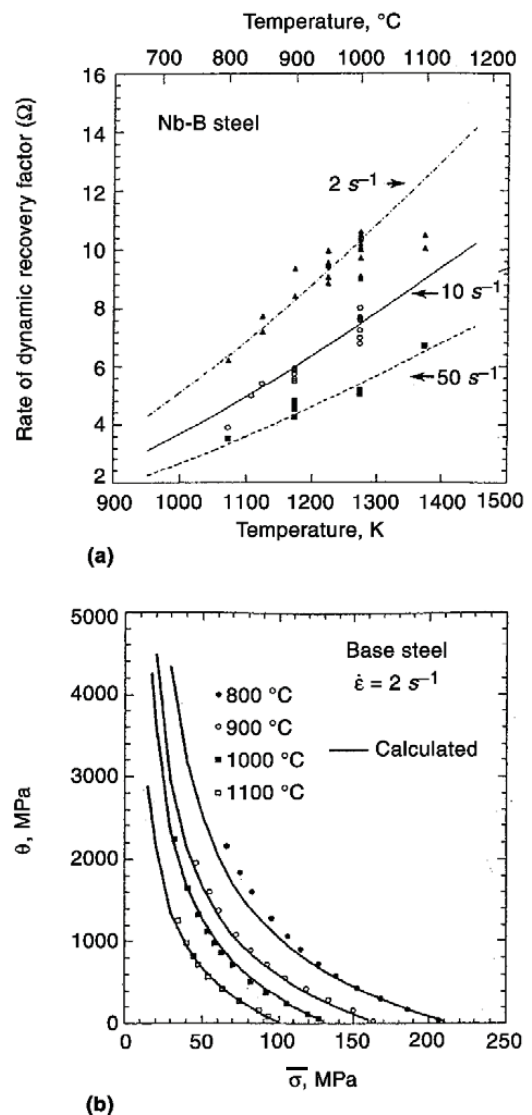


**Figure 16**

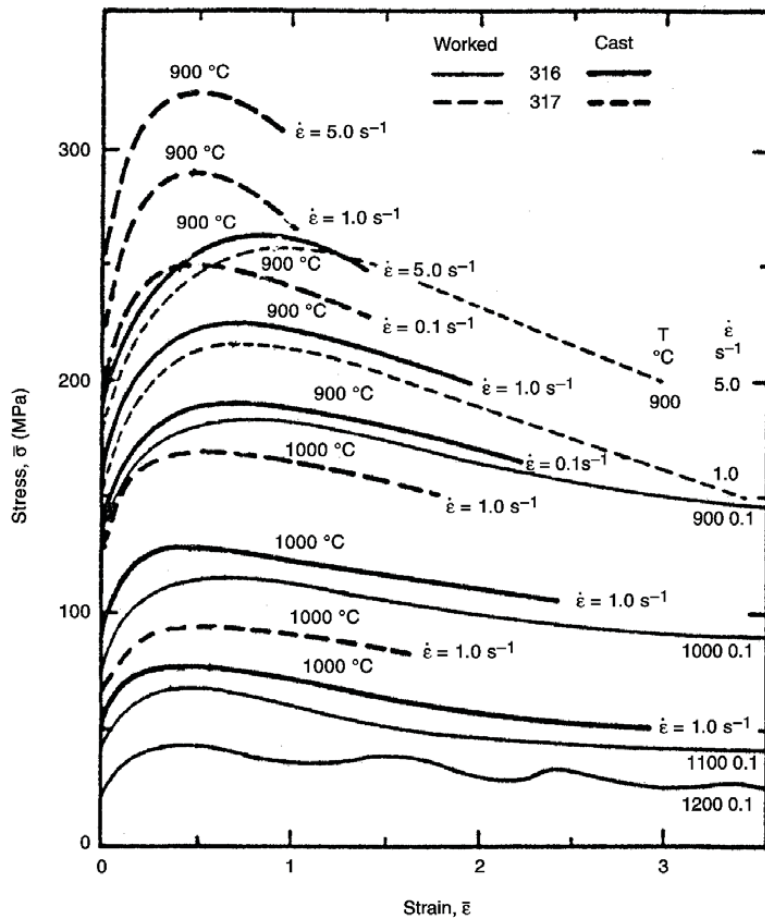


**Figure 17**

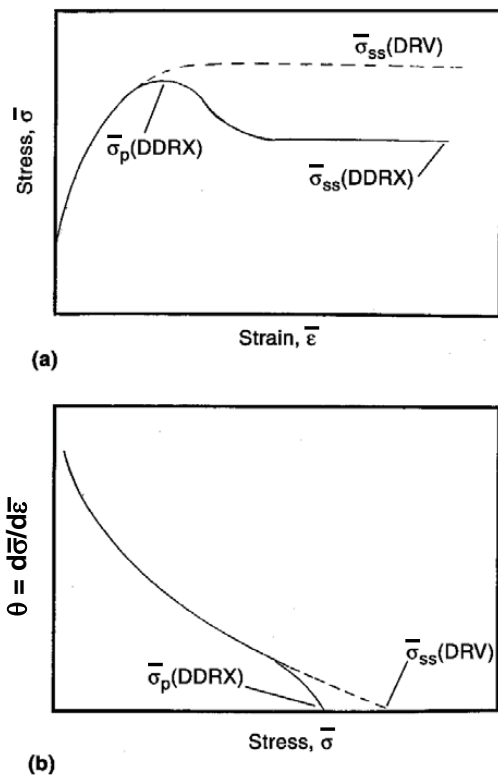
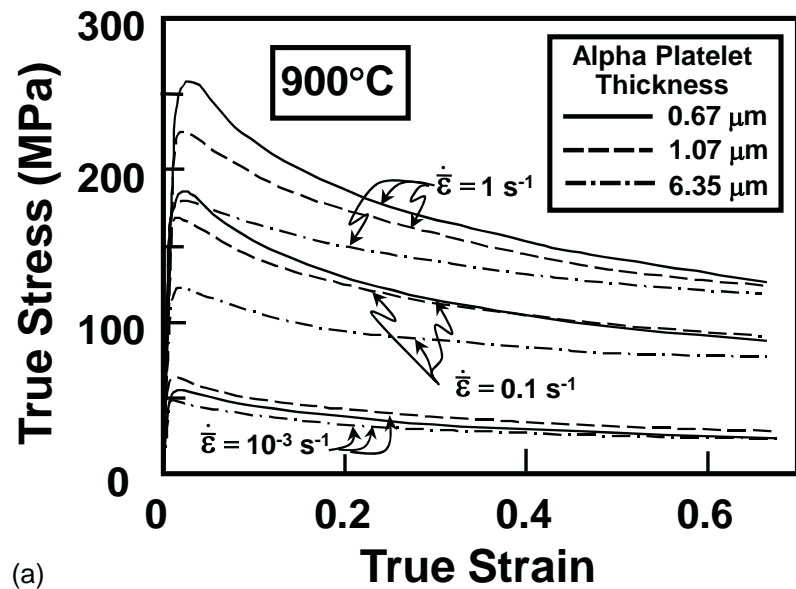
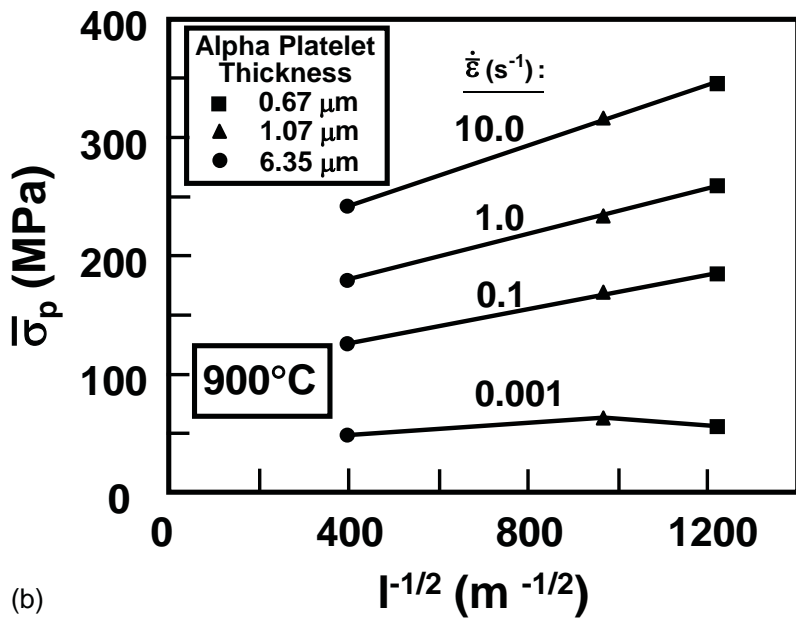


**Figure 18**



(a)



(b)

**Figure 19**

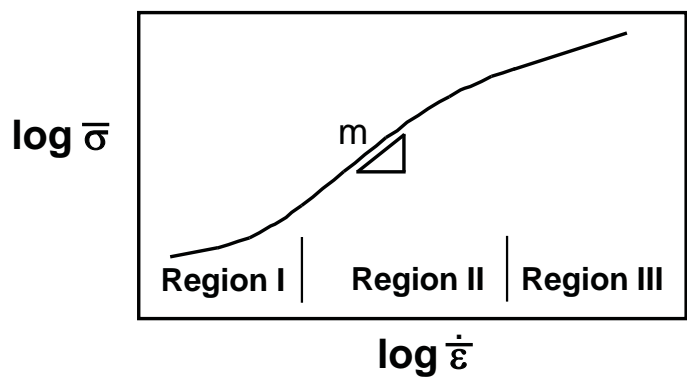


**Figure 20**

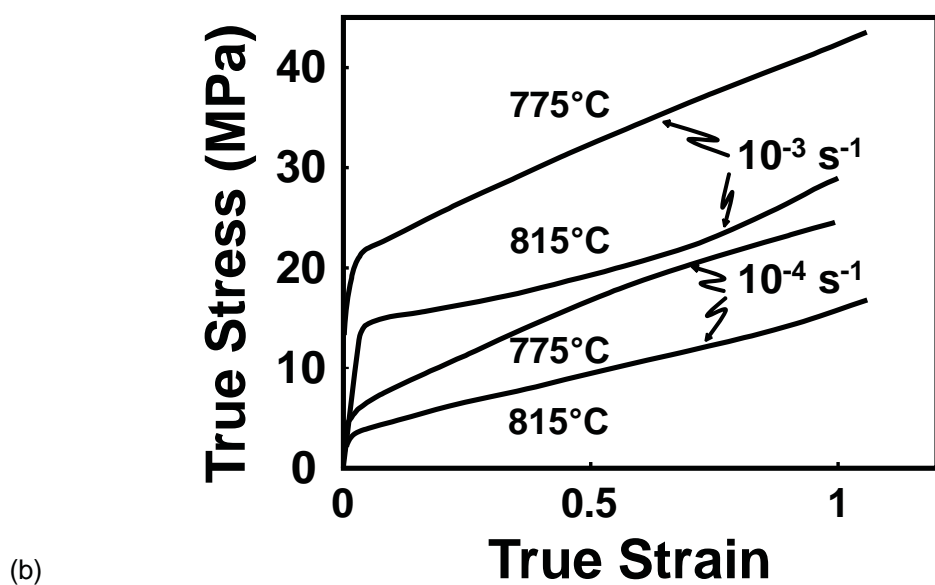
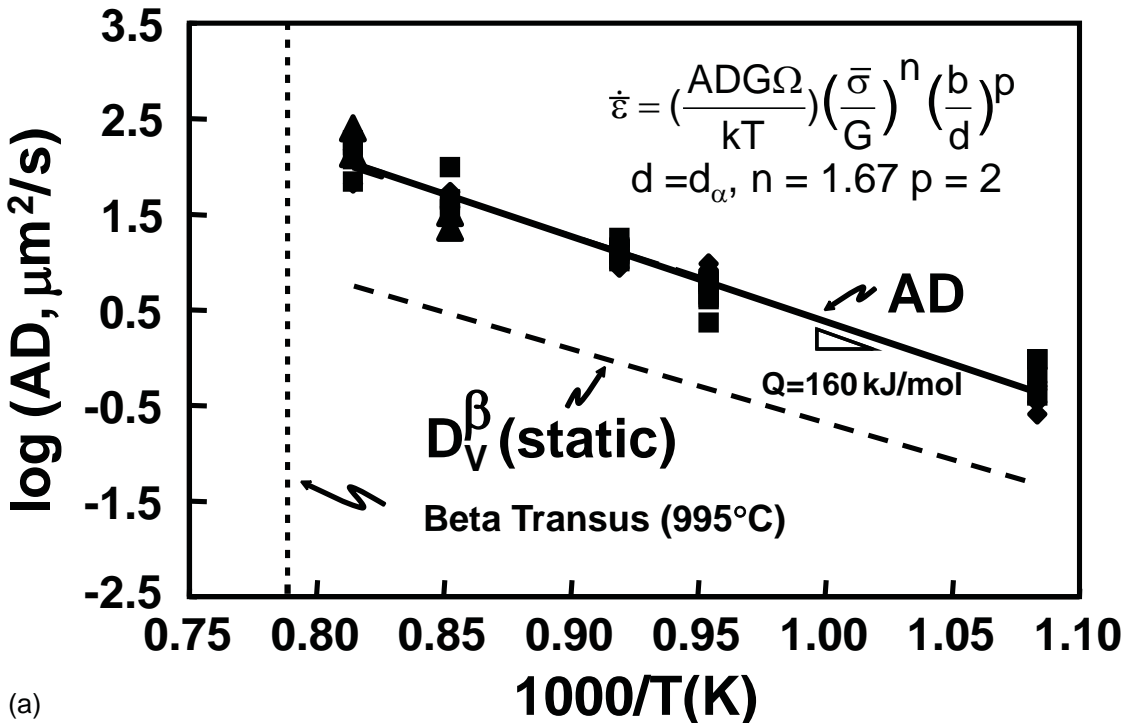


Figure 21

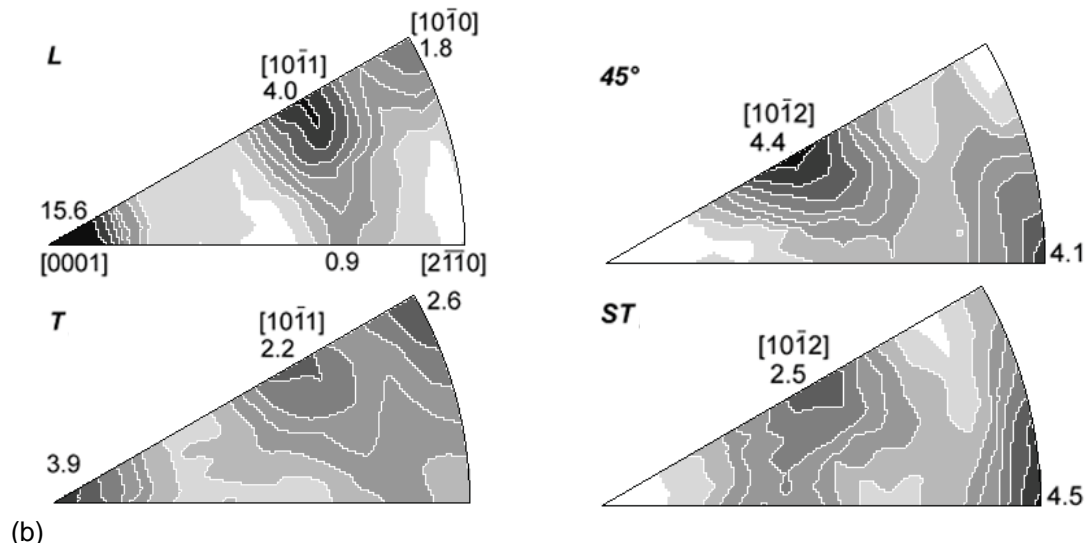
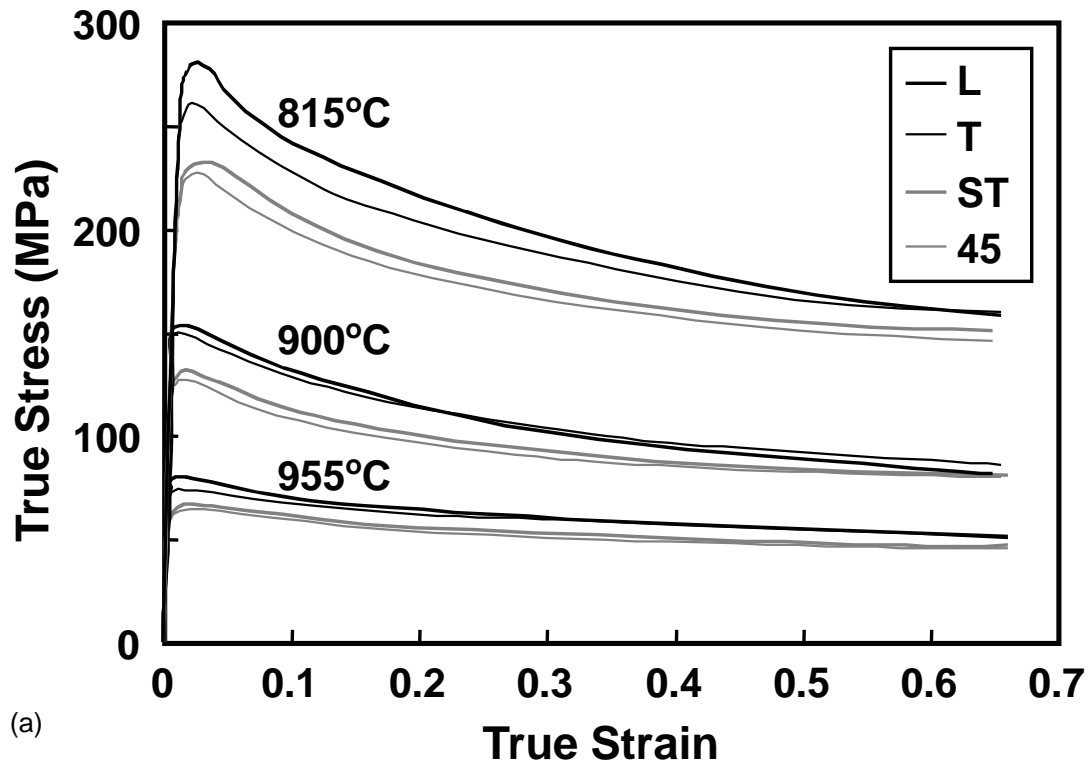


Figure 22

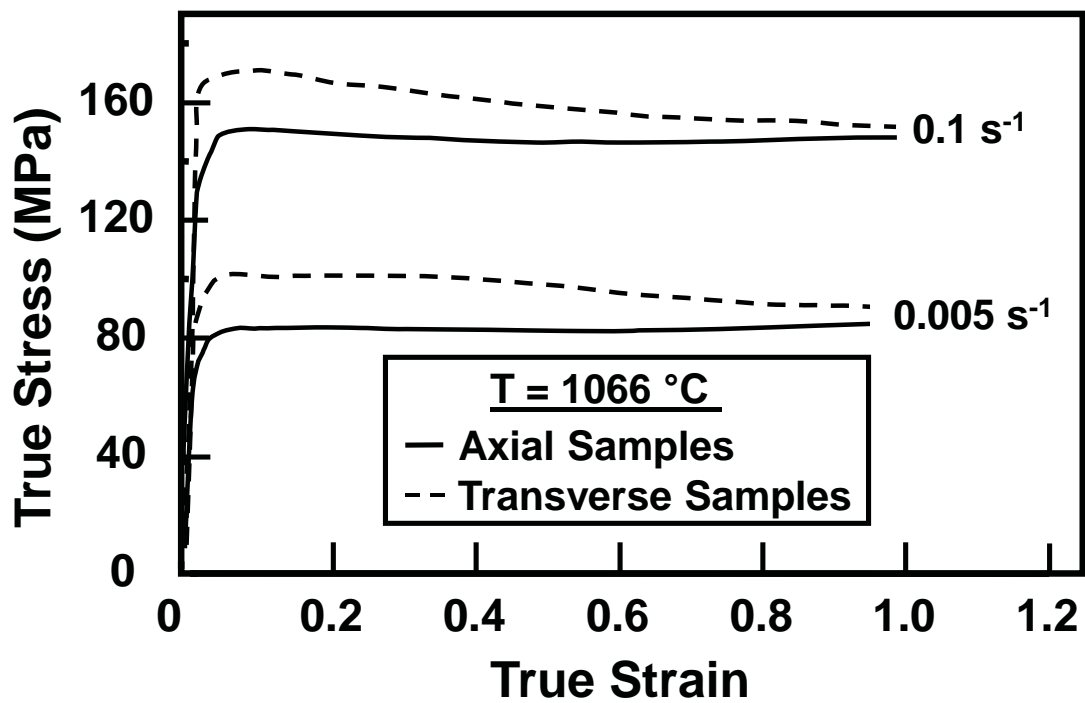


Figure 23

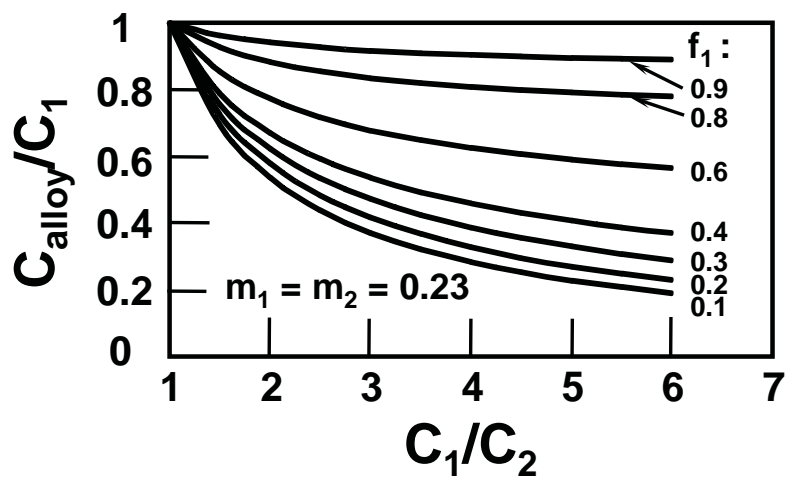


Figure 24

**Table 1.** Summary of K and n values describing the flow stress-strain relation,  $\bar{\sigma} = K(\bar{\epsilon})^n$ , for various steels

Steel	Composition(a), %											Material history(b)	Temperature		Strain rate,		K, 10 <sup>3</sup> psi	n		
	C	Mn	P	S	Si	N	Al	V	Ni	Cr	Mo		F	C	1/s	Strain range				
Armco iron	0.02	0.03	0.021	0.010	Tr							A	68	20	(c)	0.1-0.7	88.2	0.25		
1006	0.06	0.29	0.02	0.042	Tr	0.004						A	68	20	(c)	0.1-0.7	89.6	0.31		
1008	0.08	0.36	0.023	0.031	0.06	0.007						A	68	20	(c)	0.1-0.7	95.3	0.24		
	0.07	0.28			0.27							A	68	20	(c)	0.1-0.7	95.3	0.17		
1010	0.13	0.31	0.010	0.022	0.23	0.004						A	68	20	(c)	0.1-0.7	103.8	0.22		
1015	0.15	0.40	0.01	0.016	Tr							RA	32	0	30	0.2-0.7	91.4	0.116		
1015	0.15	0.40	0.01	0.016	Tr							RA	390	200	30	0.2-0.6	73.7	0.140		
1015(d)	0.15	0.40	0.045	0.045	0.25							A	68	20	1.6		113.8	0.10		
1015(d)	0.15	0.40	0.045	0.045	0.25							A	572	300	1.6		115.2	0.11		
1020	0.22	0.44	0.017	0.043	Tr	0.005						A	68	20	(c)	0.1-0.7	108.1	0.20		
1035	0.36	0.69	0.025	0.082	0.27	0.004						A	68	20	(c)	0.1-0.7	130.8	0.17		
												A	68	20	1.6		139.4	0.11		
												A	572	300	1.6		122.3	0.16		
1045(d)	0.45	0.65	0.045	0.045	0.25							A	68	20	1.6		147.9	0.11		
												A	68	20	1.5		137.9	0.14		
												A	572	300	1.6		126.6	0.15		
1050(e)	0.51	0.55	0.016	0.041	0.28	0.0062	0.03					A	68	20	(c)	0.1-0.7	140.8	0.16		
1060												A	68	20	1.6		163.5	0.09		
												A	68	20	1.5		157.8	0.12		
2317(e)	0.19	0.55	0.057	0.023	0.26	0.016						A	68	20	(c)	0.2-1.0	111.2	0.170		
5115	0.14	0.53	0.028	0.027	0.37					0.71		A	68	20	(c)	0.1-0.7	115.2	0.18		
												A	68	20	1.6		123.7	0.09		
												A	572	300	1.6		102.4	0.15		
5120(e)	0.18	1.13	0.019	0.023	0.27					0.86		A	68	20	(c)	0.1-0.7	126.6	0.18		
												A	68	20	1.6		116.6	0.09		
												A	572	300	1.6		98.1	0.16		
5140	0.41	0.67	0.04	0.019	0.35					1.07		A	68	20	(c)	0.1-0.7	125.1	0.15		
												A	68	20	1.6		133.7	0.09		
												A	572	300	1.6		112.3	0.12		
D2 tool steel(e)	1.60	0.45			0.24					0.46	11.70	0.75	0.59	A	68	20	(c)	0.2-1.0	191.0	0.157
L6 tool steel	0.56									0.14	1.60	1.21	0.47	A	68	20	(c)	0.2-1.0	170.2	0.128
W1-1.0C special	1.05	0.21			0.16							A	68	20	(c)	0.2-1.0	135.6	0.179		
302 SS	0.08	1.06	0.037	0.005	0.49					9.16	18.37			HRA	32	0	10	0.25-0.7	186.7	0.295
												HRA	390	200	30	0.25-0.7	129.8	0.278		
												HRA	750	400	30	0.25-0.7	92.7	0.279		
302 SS	0.053	1.08	0.027	0.015	0.27					10.2	17.8			A	68	20	(c)	0.1-0.7	210.5	0.6
304 SS(e)	0.030	1.05	0.023	0.014	0.47					10.6	18.7			A	68	20	(c)	0.1-0.7	210.5	0.6
316 SS	0.055	0.92	0.030	0.008	0.49					12.9	18.1	2.05		A	58	20	(c)	0.1-0.7	182.0	0.59
410 SS	0.093	0.31	0.026	0.012	0.33						13.8			A	68	20	(c)	0.1-0.7	119.4	0.2
												A	68	20	1.6		137.9	0.09		
431 SS	0.23	0.38	0.020	0.006	0.42					1.72	16.32			A	68	20	(c)	0.1-0.7	189.1	0.11

(a) Tr = trace. (b) A = annealed, F = forged, HR = hot rolled. (c) Low-speed testing machine; no specific rate given. (d) Composition given is nominal (analysis not given in original reference). (e) Approximate composition.

**Table 2.** Summary of K and n values describing the flow stress-strain relation,  $\bar{\sigma} = K(\bar{\epsilon})^n$ , for various aluminum alloys

Alloy	Composition, %									Material history(a)	Temperature		Strain rate,		K, $10^3$ psi	n
	Al	Cu	Si	Fe	Mn	Mg	Zn	Ti	Cr	Pb	F	C	1/s	Strain range		
1100	99.0	0.10	0.15	0.50	0.01	0.01					CD,A	32	0	10	0.25–0.7	25.2 0.304
1100	Rem	0.01	0.10	0.16	0.01	0.01	0.03				A	68	20	(b)	0.2–1.0	17.3 0.297
EC	99.5	0.01	0.092	0.23	0.026	0.033	0.01				A(c)	68	20	4	0.2–0.8	22.4 0.204
2017	Rem	4.04	0.70	0.45	0.55	0.76	0.22			0.06	A	68	20	(b)	0.2–1.0	45.2 0.180
2024(d)	Rem	4.48	0.60	0.46	0.87	1.12	0.20			0.056	A	68	20	(b)	0.2–1.0	56.1 0.154
5052	Rem	0.068	0.10	0.19	0.04	2.74	0.01	0.003			A(e)	68	20	4	0.2–0.8	29.4 0.134
5052(d)	Rem	0.09	0.13	0.16	0.23	2.50	0.05				A	68	20	(b)	0.2–1.0	55.6 0.189
5056	Rem	0.036	0.15	0.22	0.04	4.83	0.01		0.14		A(e)	68	20	4	0.2–0.7	57.0 0.130
5083	Rem	0.01	0.10	0.16	0.77	4.41	0.01	0.002	0.13		A	68	20	4	0.2–0.8	65.2 0.131
5454	Rem	0.065	0.12	0.18	0.81	2.45	<0.01	0.002			A(e)	68	20	4	0.2–0.8	49.9 0.137
6062	Rem	0.03	0.63	0.20	0.63	0.68	0.065	0.08				68	20	(b)	0.2–1.0	29.7 0.122

(a) CD = cold drawn, A = annealed. (b) Low-speed testing machine; no specific rate given. (c) Annealed for 4 h at 752 F (400 C). (d) Approximate composition. (e) Annealed for 4 h at 788 F (420 C).

**Table 3.** Summary of K and n values describing the flow stress-strain relation,  $\bar{\sigma} = K(\bar{\epsilon})^n$ , for various copper alloys

Alloy(a)	Composition(b), %								Temperature		Material history(c)	Strain rate,		K, $10^3$ psi	n
	Cu	Si	Fe	Sb	Sn	Zn	S	Pb	Ni	F	C	1/s	Strain range		
CDA110	99.94		0.0025	0.0003			0.0012	0.0012	0.001	64	18	HR,A	2.5	0.25–0.7	65.5 0.328
CDA110										68	20	F	(d)	0.2–1.0	54.0 0.275
CDA230	84.3					15.7				68	20	A	(d)	0.2–1.0	76.7 0.373
CDA260	70.8					29.2				68	20	A	(d)	0.2–1.0	98.1 0.412
CDA260	70.05		Tr		Tr	Rem				390	200	HR,A		0.25–0.7	71.7 0.414
CDA272	63.3					36.7				68	20	A	(d)	0.2–1.0	103.9 0.394
CDA377	58.6		Tr			39.6		1.7		68	20	A	(d)	0.2–1.0	115.3 0.334
CDA521(e)	91.0					9.0				68	20	F	(d)	0.2–1.0	130.8 0.486
CDA647	97.0	0.5						2.0		68	20	F	(d)	0.2–1.0	67.2 0.282
CDA757	65.1					22.4		<0.05	12.4	68	20	A	(d)	0.2–1.0	101.8 0.401
CDA794	61.7		Tr			20.6		Tr	17.5	68	20	A	(d)	0.2–1.0	107.0 0.336

(a) CDA = Copper Development Association. (b) Tr = trace. (c) HR = hot rolled, A = annealed, F = forged. (d) Low-speed testing machine; no specific rate given. (e) Approximate composition.

**Table 4.** Summary of C (ksi) and m values describing the flow stress-strain rate relation,  $\dot{\sigma} = C(\dot{\epsilon})^m$ , for steels at various temperatures (C is in  $10^3$  psi)

Steel	Material history	Strain rate range, 1/s	Strain	C	m	C	m	C	m	C	m	C	m
Test temperature, F (C):													
1015 0.15 C, trace Si, 0.40 Mn, 0.01 P, 0.015 S	Forged, annealed	0.2-30	0.2	36.8	0.112	19.9	0.105	17.0	0.045	7.2	0.137		
			0.25										
			0.4	40.6	0.121								
			0.5			21.5	0.104	18.3	0.058	6.8	0.169		
			0.6	40.0	0.121								
			0.7	39.5	0.114	21.1	0.109	18.3	0.068	5.7	0.181		
Test temperature, F (C):													
1016 0.15 C, 0.12 Si, 0.68 Mn, 0.034 S, 0.025 P	Hot rolled, annealed	1.5-100	0.10	15.6	0.092	13.4	0.100	9.9	0.124	7.5	0.143		
			0.30	22.7	0.082	18.2	0.085	15.3	0.115	9.4	0.153		
			0.50	23.7	0.087	18.2	0.105	12.7	0.146	8.5	0.191		
			0.70	23.1	0.099	16.1	0.147	11.9	0.166	7.5	0.218		
			0.05										
			0.1	16.5	0.099	13.7	0.099	9.7	0.130	7.1	0.157		
1016 0.15 C, 0.12 Si, 0.68 Mn, 0.034 S, 0.025 P	Hot rolled, annealed	0.2	20.8	0.082	16.5	0.090	12.1	0.119	9.1	0.140			
			0.3	22.8	0.085	18.2	0.088	13.4	0.109	9.5	0.148		
			0.4	23.0	0.084	18.1	0.098	12.9	0.126	9.1	0.164		
			0.5	23.9	0.088	18.1	0.109	12.5	0.141	8.2	0.189		
			0.6	23.3	0.097	16.9	0.127	12.1	0.156	7.8	0.205		
			0.7	22.8	0.104	17.1	0.127	12.4	0.151	8.1	0.196		
Test temperature, F (C):													
1018 1025 0.25 C, 0.08 Si, 0.45 Mn, 0.012 P, 0.025 S	Forged, annealed	3.5-30	0.05	25.2	0.07	15.8	0.152	11.0	0.192	9.2	0.20		
			0.25			33.7	0.004	16.2	0.075	9.3	0.077		
			0.50	41.4	-0.032	17.2	0.080	9.6	0.094				
			0.70	41.6	-0.032	17.5	0.082	8.8	0.105				
										10.8	0.21		
Test temperature, F (C):													
1045(a) 0.46 C, 0.29 Si, 0.73 Mn, 0.018 P, 0.021 S, 0.08 Cr, 0.01 Mo, 0.04 Ni	Hot rolled, as received	0.1-100	0.3/0.5/0.7	1650 (900)	1800 (890)	1800 (890)	2000 (1090)	2200 (1205)	2150 (1180)				
Test temperature, F (C):													
1055 0.55 C, 0.24 Si, 0.73 Mn, 0.014 P, 0.016 S	Forged, annealed	3.5-30		1110 (600)	1470 (860)	1830 (1000)	2010 (1100)	2190 (1200)					
						29.4	0.087	14.9	0.125	7.4	0.145		
						32.5	0.076	13.3	0.191	7.4	0.178		
						32.7	0.086	11.5	0.237	6.4	0.229		
Test temperature, F (C):													
1060(a) 0.56 C, 0.26 Si, 0.28 Mn, 0.014 S, 0.013 P, 0.12 Cr, 0.09 Ni	Hot rolled, annealed	1.5-100	0.10	18.5	0.127	13.3	0.143	10.1	0.147	7.4	0.172		
			0.30	23.3	0.114	16.9	0.123	12.6	0.135	8.9	0.158		
			0.50	23.3	0.118	16.4	0.139	12.0	0.158	8.6	0.180		
			0.70	21.3	0.122	14.9	0.161	10.4	0.193	7.8	0.207		
				16.2	0.128	10.8	0.168	8.7	0.161	6.5	0.190		
			0.10	18.3	0.127	13.2	0.145	10.1	0.149	7.5	0.165		
Test temperature, F (C):													
1050(a) 0.56 C, 0.26 Si, 0.28 Mn, 0.014 S, 0.013 P, 0.12 Cr, 0.09 Ni	Hot rolled, as received	0.2	0.05	16.2	0.128	10.8	0.168	8.7	0.161	6.5	0.190		
			0.20	21.8	0.119	16.1	0.125	12.1	0.125	8.5	0.157		
			0.30	23.3	0.114	17.1	0.125	12.8	0.132	8.8	0.164		
			0.40	23.7	0.112	16.8	0.128	12.5	0.146	8.8	0.171		
			0.50	23.6	0.110	16.6	0.133	12.7	0.143	8.7	0.176		
			0.60	22.8	0.129	17.1	0.127	11.7	0.169	8.4	0.189		
Test temperature, F (C):													
1095(a) 100 C, 0.19 Si, 0.17 Mn, 0.027 S, 0.023 P, 0.10 Cr, 0.09 Ni	Hot rolled, annealed	1.5-100	0.10	18.3	0.346	13.9	0.143	9.8	0.159	7.1	0.184		
			0.30	21.9	0.133	16.6	0.132	11.7	0.147	8.0	0.183		
			0.50	21.3	0.120	15.7	0.151	10.5	0.176	7.3	0.209		
			0.70	21.0	0.128	18.6	0.179	9.7	0.191	6.5	0.232		
Test temperature, F (C):													
1115 0.17 C, 0.153 Si, 0.62 Mn, 0.064 S, 0.032 P	Hot rolled, as received	4.4-23.1	0.105	16.3	0.088	13.0	0.105	10.9	0.112	9.1	0.123	7.6	0.115
			0.233	19.4	0.084	15.6	0.100	12.9	0.107	10.5	0.129	8.5	0.122
			0.338	20.4	0.094	17.3	0.090	14.0	0.117	11.2	0.138	8.8	0.141
			0.512	20.9	0.099	18.0	0.093	14.4	0.127	11.0	0.159	8.3	0.173
			0.695	20.9	0.105	16.9	0.122	13.6	0.150	9.9	0.198	7.6	0.196

(continued)

(a) Approximate composition.

**Table 4. (cont'd)**

Steel	Material history	Strain rate range, 1/s	Strain	C	m	C	m	C	m	C	m	C	m
Test temperature, F (C):													
Alloy steel			0.05	16.6	0.102	12.2	0.125	9.4	0.150	7.4	0.161		
0.35 C, 0.27 Si, 1.48 Mn, 0.041 S, 0.037 P, 0.05 Cr, 0.11 Ni, 0.28 Mo			0.10	19.9	0.091	14.8	0.111	11.5	0.121	8.1	0.149		
			0.20	25.0	0.094	17.6	0.094	12.5	0.100	9.4	0.139		
			0.30	24.9	0.092	19.1	0.093	14.4	0.105	10.2	0.130		
			0.40	25.0	0.088	19.6	0.095	14.5	0.112	10.4	0.129		
			0.50	25.9	0.091	19.6	0.100	14.4	0.112	10.1	0.147		
			0.60	25.9	0.094	19.5	0.105	14.2	0.122	9.7	0.159		
			0.70	25.5	0.099	19.2	0.107	12.9	0.126	9.2	0.165		
4337(a)	Hot rolled, annealed	1.5-100	0.10	22.1	0.080	16.6	0.109	12.1	0.115	8.2	0.165		
0.35 C, 0.27 Si, 0.66 Mn, 0.028 S, 0.029 P, 0.59 Cr, 2.45 Ni, 0.59 Mo			0.30	28.1	0.077	20.8	0.098	15.0	0.113	10.7	0.138		
			0.50	29.2	0.075	21.8	0.086	15.7	0.112	11.3	0.133		
			0.70	28.1	0.080	21.3	0.102	15.5	0.122	11.3	0.135		
924(a)	Hot rolled, annealed	1.5-100	0.10	22.9	0.109	17.1	0.105	11.8	0.152	8.6	0.168		
0.61 C, 1.58 Si, 0.94 Mn, 0.038 S, 0.035 P, 0.12 Cr, 0.27 Ni, 0.06 Mo			0.30	28.2	0.101	20.4	0.108	14.3	0.140	10.1	0.162		
			0.50	27.8	0.104	20.0	0.120	13.8	0.154	9.1	0.193		
			0.70	25.8	0.112	18.2	0.146	11.8	0.179	7.5	0.225		
50100(a)			0.05	16.1	0.155	12.4	0.155	8.2	0.175	6.3	0.199		
1.00 C, 0.19 Si, 0.17 Mn, 0.027 S, 0.023 P, 0.10 Cr, 0.09 Ni			0.10	18.6	0.145	14.1	0.142	9.5	0.164	6.8	0.191		
			0.20	20.9	0.135	15.9	0.131	11.4	0.141	8.1	0.167		
			0.30	21.8	0.135	16.6	0.134	11.7	0.142	8.0	0.174		
			0.40	22.0	0.154	16.8	0.134	11.2	0.155	8.4	0.164		
			0.50	21.5	0.131	15.6	0.150	11.1	0.158	7.4	0.199		
			0.60	21.3	0.132	14.6	0.169	10.0	0.184	7.0	0.212		
			0.70	20.9	0.121	13.5	0.176	9.7	0.182	6.7	0.220		
S2100	Hot rolled, annealed	1.5-100	0.10	20.9	0.128	14.3	0.146	9.5	0.169	6.7	0.208		
1.06 C, 0.22 Si, 0.46 Mn, 0.019 S, 0.021 P, 1.41 Cr, 0.17 Ni			0.30	25.5	0.107	17.7	0.127	12.0	0.143	8.3	0.171		
			0.50	25.9	0.107	17.7	0.129	12.3	0.148	8.3	0.178		
			0.70	25.3	0.131	16.8	0.134	12.0	0.148	7.7	0.192		
Test temperature, F(C):													
Mn-Si steel			0.05	19.2	0.117	14.8	0.119	9.7	0.172	7.5	0.181		
0.61 C, 1.58 Si, 0.94 Mn, 0.038 S, 0.025 P, 0.12 Cr, 0.27 Ni, 0.06 Mo			0.10	22.6	0.112	17.1	0.108	11.8	0.151	8.7	0.166		
			0.20	25.7	0.105	19.5	0.101	13.5	0.159	9.7	0.180		
			0.30	27.6	0.108	20.5	0.109	14.8	0.126	10.0	0.161		
			0.40	27.6	0.114	20.2	0.114	14.4	0.141	9.5	0.179		
			0.50	27.2	0.113	19.8	0.125	14.1	0.144	9.1	0.188		
			0.60	26.0	0.121	18.8	0.137	12.8	0.162	8.2	0.209		
			0.70	24.7	0.130	17.8	0.132	11.9	0.178	7.5	0.223		
Cr-Si steel			0.05	19.9	0.118	22.9	0.104	15.1	0.167	10.0	0.205		
0.47 C, 3.74 Si, 0.58 Mn, 8.20 Cr, 20 Ni			0.10	19.9	0.126	25.6	0.120	16.8	0.162	11.1	0.189		
			0.20	19.9	0.143	27.6	0.121	18.5	0.153	11.9	0.184		
			0.30	19.9	0.144	28.4	0.119	15.1	0.148	12.1	0.182		
			0.40	19.3	0.150	28.2	0.125	18.9	0.150	12.1	0.173		
			0.50	18.5	0.155	26.6	0.132	18.5	0.155	11.8	0.182		
			0.60	17.5	0.150	25.2	0.142	17.5	0.160	11.5	0.182		
			0.70	16.1	0.163	23.3	0.158	16.1	0.162	10.2	0.192		
D8(a)	Hot rolled, annealed	1.5-100	0.10	39.2	0.087	29.0	0.108	21.0	0.125	14.6	0.121		
2.23 C, 0.43 Si, 0.37 Mn, 13.10 Cr, 0.33 Ni			0.30	45.7	0.087	30.4	0.114	21.0	0.159	13.9	0.130		
			0.50	39.7	0.101	27.1	0.125	18.4	0.155	12.3	0.124		
			0.70	33.3	0.131	22.5	0.145	15.3	0.168	10.7	0.208		
Test temperature, F (C):													
H-13			0.10	19.1	0.252	10.2	0.305	6.0	0.373	4.8	0.374		
0.39 C, 1.02 Si, 0.60 Mn, 0.016 P, 0.020 S, 5.29 Cr, 0.04 Ni, 1.25 Mo, 0.027 N, 0.83 V			0.2	20.1	0.179	13.7	0.275	8.2	0.341	9.0	0.255		
			0.3	31.0	0.179	15.1	0.265	10.8	0.308	11.6	0.267		
			0.4	25.9	0.204	12.5	0.295	12.5	0.287	11.8	0.269		
Test temperature, F (C):													
H-26(0)	Hot rolled, annealed	1.5-100	0.10	45.7	0.058	37.4	0.072	26.2	0.106	18.7	0.125		
0.80 C, 0.28 Si, 0.33 Mn, 4.39 Cr, 0.18 Ni, 0.55 Mo, 18.40 W, 1.54 V			0.20	49.6	0.075	38.1	0.087	26.0	0.121	18.3	0.140		
			0.30	44.6	0.096	32.7	0.102	22.6	0.131	16.2	0.151		
			0.40	39.1	0.115	27.9	0.124	20.1	0.148	13.8	0.162		

(continued)

(a) Approximate composition.

**Table 4. (cont'd)**

Steel	Material history	Strain rate range, 1/s	Strain	C	m	C	m	C	m	C	m	C	m
Test temperature, F (C):													
301 SS(a)	Hot rolled, annealed	0.8-100	0.25		40.5	0.051	16.3	0.117	7.6	0.161			
0.08 C, 0.93 Si, 1.10 Mn, 0.009 P, 0.014 S, 16.9 Cr, 5.6 Ni, 0.31 Mn, 0.9 Al, 0.02 N, 0.068 Se			0.50		39.3	0.062	17.8	0.108	7.6	0.177			
			0.70		37.8	0.069	17.4	0.102	6.6	0.192			
302 SS	Hot rolled, annealed	310-460	0.25	26.5	0.147	25.1	0.129	11.0	0.305	4.6	0.281		
0.07 C, 0.71 Si, 1.07 Mn, 0.02 P, 0.005 S, 18.34 Cr, 9.56 Ni			0.40	31.3	0.153	30.0	0.121	13.5	0.388	4.7	0.284		
			0.60	17.5	0.270	45.4	0.068	15.8	0.161	4.1	0.310		
303 SS	Hot rolled, annealed	0.2-30	0.25	52.2	0.031	36.6	0.042	23.1	0.040	12.8	0.082		
0.08 C, 0.49 Si, 1.06 Mn, 0.037 P, 0.005 S, 18.37 Cr, 9.16 Ni			0.40	58.9	0.021	40.4	0.022	24.7	0.050	12.6	0.083		
			0.60	65.2	0.020	41.8	0.080	24.9	0.053	13.5	0.091		
			0.70	64.0	0.023	42.0	0.031	24.7	0.052	13.4	0.096		
Test temperature, F (C):													
302 SS		1.5-100	0.05	24.6	0.023	15.8	0.079	12.7	0.093	9.7	0.139		
0.07 C, 0.42 Si, 0.68 Mn, 0.025 P, 0.008 Ni			0.10	28.4	0.021	21.2	0.068	15.6	0.091	11.1	0.127		
			0.20	23.4	0.031	25.2	0.067	18.1	0.089	12.5	0.120		
			0.30	35.3	0.042	26.3	0.074	19.5	0.089	13.5	0.115		
			0.40	35.6	0.055	26.9	0.084	19.9	0.094	14.2	0.110		
			0.50	35.6	0.060	27.0	0.093	19.6	0.098	14.2	0.115		
			0.60	34.1	0.065	26.4	0.092	19.3	0.102	13.8	0.118		
			0.70	23.5	0.072	25.7	0.102	18.9	0.158	13.9	0.120		
Test temperature, F (C):													
303 SS	Hot drawn, annealed	200-525	0.25		39.4	0.079				8.7	0.184		
0.13 C, 0.42 Si, 1.30 Mn, 0.025 P, 0.008 S, 22.30 Cr, 12.99 Ni			0.40		45.1	0.074				9.6	0.178		
			0.60		48.1	0.076				9.5	0.185		
310 SS	Hot drawn, annealed	310-460	0.25	50.3	0.080	32.3	0.127	27.5	0.101	12.0	0.154		
0.12 C, 1.26 Si, 1.56 Mn, 0.01 P, 0.009 S, 25.49 Cr, 21.28 Ni			0.40	56.5	0.080	32.2	0.142	22.8	0.143	10.8	0.175		
			0.60	61.8	0.067	21.9	0.212	9.7	0.284	4.5	0.326		
316 SS	Hot drawn, annealed	310-460	0.25	13.5	0.263	32.2	0.149	6.4	0.217	8.0	0.204		
0.06 C, 0.52 Si, 1.40 Mn, 0.005 P, 0.005 S, 17.25 Cr, 12.23 Ni, 2.17 Mo			0.40	28.8	0.162	26.8	0.138	3.7	0.435	7.4	0.227		
			0.60	39.3	0.128	30.1	0.133	6.1	0.365	6.5	0.254		
403 SS	Hot rolled, annealed	0.8-100	0.25		26.3	0.079	15.4	0.125	7.3	0.157			
0.16 C, 0.37 Si, 0.44 Mn, 0.024 P, 0.007 S, 12.62 Cr			0.50		26.9	0.076	15.0	0.142	7.8	0.152			
			0.70		24.6	0.090	15.3	0.158	7.5	0.155			
SS	Hot rolled, annealed	0.8-100	0.25		28.7	0.082	17.2	0.082	11.9	0.079			
0.12 C, 0.12 Si, 0.29 Mn, 0.014 P, 0.016 S, 12.11 Cr, 0.50 Ni, 0.45 Mo			0.50		29.1	0.093	20.7	0.073	11.6	0.117			
			0.70		28.7	0.096	22.5	0.067	11.2	0.131			
SS	Hot rolled, annealed	3.5-30	0.25					19.5	0.099	8.9	0.128	28.3	0.114
0.08 C, 0.45 Si, 0.43 Mn, 0.031 P, 0.005 S, 17.38 Cr, 0.31 Ni			0.50					22.3	0.097	9.5	0.145	24.9	0.105
			0.70					23.2	0.098	9.2	0.158	37.1	0.107
Test temperature, F (C):													
Maraging 300				1600 (870)		1700 (925)		1800 (980)		2000 (1095)		2100 (1150)	
				43.4	0.077	36.4	0.095	30.6	0.113	21.5	0.145	18.0	0.165
Maraging 300				2200 (1205)									
				12.8	0.185								

(a) Approximate composition.

**Table 5.** Summary of C (ksi) and m values describing the flow stress-strain rate relation,  $\bar{\sigma} = C(\dot{\varepsilon})^m$ , for aluminum alloys at various temperatures

Alloy	Material history	Strain rate range, 1/s	Strain	C	m	C	m	C	m	C	m	C	m	
		Test temperature, F (C):		390 (200)		570 (300)		750 (400)		930 (500)		1110 (600)		
Super-pure 99.98 Al, 0.0017 Cu, 0.0026 Si, 0.0033 Fe, 0.005 Mn	Cold rolled, annealed 1/2 h at 1110 F	0.4-311		0.288	5.7	0.110	4.3	0.120	2.8	0.140	1.6	0.155	0.6	0.250
				2.88	8.7	0.090	4.9	0.095	2.8	0.125	1.6	0.175	0.6	0.215
EC	Annealed 3 h at 750 F	0.25-63			465 (240)		645 (360)		825 (480)					
1100	Cold drawn, annealed	0.25-40		0.20	10.9	0.056	5.9	0.141	3.4	0.168				
				0.40	12.3	0.059	6.3	0.146	3.3	0.169				
				0.60	13.1	0.057	6.4	0.147	3.2	0.173				
				0.80	13.8	0.054	6.7	0.135	3.4	0.161				
		Test temperature, F (C):		390 (200)		750 (400)		930 (500)						
1100(a)	Extruded annealed 1 h at 750 F	4-40		0.25	9.9	0.066	4.2	0.115	2.1	0.211				
				0.50	11.6	0.071	4.4	0.132	2.1	0.227				
				0.70	12.2	0.075	4.5	0.141	2.1	0.224				
		Test temperature, F (C):		360 (150)		480 (250)		660 (350)		840 (450)		1020 (550)		
2017	Cold drawn, annealed	0.2-30		0.105	11.4	0.022	9.1	0.026	6.3	0.055	3.9	0.100	2.2	0.130
				0.225	13.5	0.022	10.5	0.031	6.9	0.061	4.3	0.098	2.4	0.130
				0.350	15.0	0.021	11.4	0.025	7.2	0.073	4.5	0.100	2.5	0.141
				0.572	16.1	0.036	11.9	0.041	7.5	0.084	4.4	0.116	2.4	0.156
				0.695	17.0	0.026	12.3	0.041	7.4	0.088	4.3	0.130	2.4	0.155
		Test temperature, F (C):		390 (200)		750 (400)		930 (500)						
2017(a)	Solution treated 1 h at 250 F, water quenched annealed 4 h at 750 F	0.4-311		0.115	10.8	0.695	9.1	0.100	7.5	0.110	6.2	0.145	5.1	0.155
				2.660	10.0	0.100	9.2	0.100	7.7	0.080	6.8	0.090	4.6	0.155
		Test temperature, F (C):		570 (300)		660 (350)		750 (400)		840 (450)		930 (500)		
5052	Annealed 3 h at 750 F	0.25-63		0.20	14.3	0.038	8.9	0.067	5.6	0.125				
				0.40	15.9	0.035	9.3	0.071	5.3	0.130				
				0.60	16.8	0.035	9.0	0.068	5.1	0.134				
				0.80	17.5	0.038	9.4	0.068	5.6	0.125				
5056	Annealed 3 h at 750 F	0.25-63		0.20	42.6	-0.032	20.9	0.128	11.7	0.200				
				0.40	44.0	-0.032	20.8	0.136	10.5	0.205				
				0.60	44.9	-0.031	19.9	0.143	10.3	0.202				
				0.70	45.6	-0.034	20.3	0.144	10.3	0.203				
5083	Annealed 3 h at 750 F	0.25-63		0.20	43.6	-0.005	20.5	0.095	9.3	0.182				
				0.40	43.6	-0.051	19.7	0.106	8.3	0.203				
				0.60	41.9	0.003	18.8	0.111	8.5	0.201				
				0.80	40.2	0.052	19.1	0.105	9.7	0.151				
5454	Annealed 3 h at 750 F	0.25-63		0.20	33.6	-0.055	16.8	0.093	10.8	0.182				
				0.40	35.0	-0.009	16.3	0.104	10.7	0.188				
				0.60	36.9	-0.009	16.0	0.102	10.0	0.191				
				0.80	37.0	-0.009	16.2	0.097	10.2	0.182				
		Test temperature, F (C):		750 (400)		840 (450)		930 (500)		1020 (550)				
7075(a)	Solution treated 1 h at 870 F, water quenched, aged at 285 F for 16 h	0.4-311		0.115	10.0	0.090	6.0	0.115	3.9	0.150	2.9	0.170		
				2.66	9.7	0.115	6.2	0.120	4.8	0.115	2.7	0.115		

(a) Approximate composition.

**Table 6.** Summary of C (ksi) and m values describing the flow stress-strain rate relation,  $\dot{\sigma} = C(\dot{\epsilon})^m$ , for copper alloys at various temperatures

Alloy	Material history	Strain rate range, 1/s	Strain	Test temperature, F (C):				Test temperature, F (C):				Test temperature, F (C):			
				C	m	C	m	C	m	C	m	C	m	C	m
Copper	Cold drawn, annealed 2 h	4-40	0.105	20.2	0.016	17.0	0.010	12.7	0.050	7.6	0.095	4.7	0.134		
0.018 P, 0.0010 Ni, 0.0003 Sn, 0.0002 Sb, 0.0005 Pb, 0.0010 Fe, 0.0020 Mn < 0.0005 Mg, < 0.0005 As, < 0.0001 Bi, 0.0014 Si, less than 0.003 O <sub>p</sub> , Sn + Te not detected			0.23	26.5	0.018	22.5	0.004	16.8	0.043	9.7	0.097	6.3	0.110		
			0.338	30.2	0.017	28.1	0.008	18.9	0.041	10.0	0.128	6.1	0.154		
			0.512	32.2	0.025	26.6	0.014	19.4	0.066	8.3	0.186	5.5	0.195		
			0.695	24.4	0.024	26.8	0.021	19.0	0.078	8.2	0.182	5.2	0.190		
OFHC Copper															
CDA 110	Hot rolled, annealed	0.25-40	0.25	23.0	0.046	12.9	0.136	6.6	0.160						
99.64 Cu, 0.0003 Sb, 0.0012 Pb, 0.0012 Sn, 0.0025 Fe, 0.001 Ni			0.50	27.4	0.049	15.7	0.150	6.9	0.168						
			0.70	28.8	0.057	13.3	0.163	6.8	0.176						
CDA 220	Extruded, cold drawn 30%; annealed 650 C, 90 min	0.1-10	0.25	41.0	0.017	34.1	0.018	22.6	0.061	11.2	0.134				
90.06 Cu, 0.053 Fe, 0.004 Pb, 0.002 Sn, Rem Zn			0.50	46.7	0.029	39.9	0.032	24.4	0.084	11.0	0.156				
			0.70	48.1	0.034	40.7	0.036	24.6	0.086	11.4	0.140				
CDA 260	Hot rolled, annealed	3.5-30	0.25			34.9	0.036	16.0	0.154	7.1	0.144				
70.05 Cu, trace Fe + Sn, Rem Zn			0.50			42.3	0.031	14.8	0.237	7.0	0.148				
			0.70			42.4	0.045	14.3	0.228	6.3	0.151				
CDA 280	Hot rolled, annealed	3.5-10	0.25	49.0	0.028	26.9	0.083	7.6	0.189	3.1	0.228				
50.44 Cu, 0.01 Pb, 0.02 Fe, trace Sn, Rem Zn			0.50	58.6	0.027	28.6	0.075	5.4	0.281	2.8	0.239				
			0.70	60.3	0.027	26.7	0.081	4.7	0.291	2.7	0.220				
CDA 365	Hot rolled, annealed	3.5-30	0.25	45.8	0.038	28.6	0.065	9.8	0.106	2.4	0.166				
59.78 Cu, 0.90 Pb, 0.02 Fe, trace Sn, Rem Zn			0.50	57.2	0.032	28.9	0.083	8.5	0.137	2.1	0.197				
			0.70	59.1	0.035	26.6	0.078	8.4	0.113	1.8	0.222				

**Table 7.** Summary of C (ksi) and m values describing the flow stress-strain rate relation,  $\dot{\sigma} = C(\dot{\varepsilon})^m$ , for titanium alloys at various temperatures

Alloy	Material history	Strain rate range, 1/s	Strain	C	m	C	m	C	m	C	m	C	m	C	m	C	m
Test temperature, F (C):																	
Type 1	Annealed	0.25-16.0	0.2	92.8	0.029	60.9	0.046	39.8	0.074	25.3	0.097	12.8	0.167	5.4	0.280	3.0	0.387
0.04 Fe, 0.02 C, 0.005 H <sub>2</sub> , 0.01 N <sub>2</sub> , 0.04 O <sub>2</sub> , Rem Ti	15 min at 1200 F in high vacuum	0.4	113.7	0.029	75.3	0.056	48.8	0.061	29.6	0.115	14.6	0.181	5.5	0.248	3.6	0.289	
Type 2	Annealed	0.25-16.0	0.2	129.6	0.029	82.2	0.056	53.9	0.049	32.1	0.105	14.9	0.195	5.5	0.245	3.5	0.289
0.15 Fe, 0.02 C, 0.005 H <sub>2</sub> , 0.02 N <sub>2</sub> , 0.12 O <sub>2</sub> , Rem Ti	15 min at 1200 F in high vacuum	0.6	142.5	0.027	87.7	0.058	56.3	0.042	32.7	0.099	15.4	0.180	5.9	0.185	3.2	0.264	
Test temperature, F (C):																	
Unalloyed	Hot rolled, annealed 800 C, 0.032% H, Rem Ti	0.1-10	0.25	23.4	0.062	14.3	0.115	8.2	0.236	1.8	0.324						
			0.50	27.9	0.066	17.8	0.111	10.0	0.242	2.1	0.326						
			0.70	30.1	0.065	20.0	0.098	12.2	0.185	2.5	0.316						
Test temperature, F (C):																	
Ti-5Al-2.5 Sn	Annealed	0.25-16.0	0.1	173.6	0.046	125.6	0.028	97.6	0.028								
5.1 Al, 3.5 Sn, 0.05 Fe, 0.02 C, 0.01 H <sub>2</sub> , 0.03 N <sub>2</sub> , 0.1 O <sub>2</sub> , Rem Ti	30 min at 1470 F in high vacuum	0.2	197.9	0.048	138.8	0.022	107.4	0.026	85.1	0.025	58.5	0.034	44.3	0.069	5.4	0.308	
		0.3	215.6	0.046	147.4	0.021	112.5	0.027	92.8	0.020							
		0.4	230.6	0.039	151.4	0.022	116.0	0.022	95.6	0.019	58.7	0.040	44.8	0.082	5.1	0.294	
		0.5								96.7	0.021						
		0.6								95.6	0.024	55.6	0.042	43.0	0.078	5.2	0.284
		0.8									50.2	0.033	39.1	0.073	5.2	0.264	
		0.9									46.8	0.025					
		1.0										35.2	0.056	5.3	0.280		
Ti-5Al-4V	Annealed	0.25-16.0	0.1	202.3	0.017	143.8	0.026	119.4	0.025								
6.4 Al, 4.0 V, 0.14 Fe, 0.05 C, 0.01 H <sub>2</sub> , 0.015 N <sub>2</sub> , 0.1 O <sub>2</sub> , Rem Ti	120 min at 1200 F	0.2	209.7	0.015	151.0	0.021	127.6	0.022	94.6	0.054	51.3	0.146	23.3	0.143	9.5	0.131	
		0.3	206.0	0.015	152.0	0.017	126.2	0.017	91.2	0.073							
		0.4								118.7	0.014	84.6	0.079	39.8	0.175	21.4	0.147
		0.5									77.9	0.080					
		0.6										30.4	0.203	20.0	0.161	9.6	0.118
		0.8										26.6	0.199	19.5	0.172	9.3	0.154
		0.9										24.9	0.201				
		1.0										20.3	0.146	8.9	0.192		
Test temperature, F (C):																	
Ti-6Al-4V				1550 (843)		1750 (954)		1800 (982)									
				38.0	0.064	12.3	0.24	9.4	0.29								
Test temperature, F (C):																	
Ti-13V-11Cr-3Al	Annealed	0.25-16.0	0.1	173.1	0.041												
3.6 Al, 14.1 V, 10.6 Cr, 0.27 Fe, 0.02 C, 0.014 H <sub>2</sub> , 0.08 N <sub>2</sub> , 0.11 O <sub>2</sub> , Rem Ti	30 min at 1290 F in high vacuum	0.2	188.2	0.037	150.5	0.030	135.5	0.025	118.4	0.040	65.4	0.097	44.6	0.147	32.4	0.153	
		0.3	202.3	0.034													
		0.4	215.2	0.028	174.2	0.024	158.9	0.030	107.5	0.039	59.5	0.096	42.1	0.139	30.9	0.142	
		0.5	226.3	0.026	181.1	0.023											
		0.6			183.5	0.026	147.9	0.046	92.8	0.045	56.7	0.088	40.9	0.127	29.2	0.153	
		0.7			181.4	0.029							136.3	0.045	84.7	0.086	
		0.8											52.9	0.080			
		0.9													38.8	0.127	
		1.0													28.0	0.159	